Title	Systematic study of charged-pion and kaon femtoscopy in Au + Au collisions at $\sqrt{s_{NN}}=200$ GeV
Author(s)	Adare A., Hasegawa Shoichi, Imai Kenichi, Sako Hiroyuki, Sato Susumu, Tanida Kiyoshi, PHENIX Collaboration, 493 of others
Citation	Physical Review C, 92(3), p.034914_1-034914_21
Text Version	Publisher's Version
URL	https://jopss.jaea.go.jp/search/servlet/search?5054477
DOI	https://doi.org/10.1103/PhysRevC.92.034914
Right	© 2015 The American Physical Society

Systematic study of charged-pion and kaon femtoscopy in Au + Au collisions at $\sqrt{s_{NN}} = 200$ GeV

A. Adare,[13] S. Afanasiev,[31] C. Aidala,[44,45] N. N. Ajitanand,[64] Y. Akiba,[58,59] H. Al-Bataineh,[52] J. Alexander,[64] M. Alfred,[24] K. Aoki,[33,36,58] N. Apadula,[29,65] Y. Aramaki,[12] H. Asano,[36,58] E. T. Atomssa,[37] R. Averbeck,[65] T. C. Awes,[54] B. Azmoun,[7] V. Babintsev,[25] M. Bai,[6] G. Baksay,[20] L. Baksay,[20] N. S. Bandara,[44] B. Bannier,[65] K. N. Barish,[8] B. Bassalleck,[51] A. T. Basye,[1] S. Bathe,[5,8,59] V. Baublis,[57] C. Baumann,[7,46] A. Bazilevsky,[7] M. Beaumier,[8] S. Beckman,[13] S. Belikov,[7,*] R. Belmont,[13,45,69] R. Bennett,[65] A. Berdnikov,[61] Y. Berdnikov,[61] A. A. Bickley,[13] D. S. Blau,[35] J. S. Bok,[52,73] K. Boyle,[59,65] M. L. Brooks,[40] J. Bryslawskyj,[5] H. Buesching,[7] V. Bumazhnov,[25] G. Bunce,[7,59] S. Butsyk,[40] C. M. Camacho,[40] S. Campbell,[14,29,65] C.-H. Chen,[59,65] C. Y. Chi,[14] M. Chiu,[7] I. J. Choi,[26,73] J. B. Choi,[10] R. K. Choudhury,[4] P. Christiansen,[42] T. Chujo,[68] P. Chung,[64] O. Chvala,[8] V. Cianciolo,[54] Z. Citron,[65,71] B. A. Cole,[14] M. Connors,[65] P. Constantin,[40] M. Csanád,[18] T. Csörgő,[72] T. Dahms,[65] S. Dairaku,[36,58] I. Danchev,[69] D. Danley,[53] K. Das,[21] A. Datta,[44,51] M. S. Daugherity,[1] G. David,[7] K. DeBlasio,[51] K. Dehmelt,[20,65] A. Denisov,[25] A. Deshpande,[59,65] E. J. Desmond,[7] O. Dietzsch,[62] A. Dion,[65] P. B. Diss,[43] J. H. Do,[73] M. Donadelli,[62] O. Drapier,[37] A. Drees,[65] K. A. Drees,[6] J. M. Durham,[40,65] A. Durum,[25] D. Dutta,[4] S. Edwards,[21] Y. V. Efremenko,[54] F. Ellinghaus,[13] T. Engelmore,[14] A. Enokizono,[39,58,60] H. En'yo,[58,59] S. Esumi,[68] B. Fadem,[47] N. Feege,[65] D. E. Fields,[51] M. Finger,[9] M. Finger, Jr.,[9] F. Fleuret,[37] S. L. Fokin,[35] Z. Fraenkel,[71,*] J. E. Frantz,[53,65] A. Franz,[7] A. D. Frawley,[21] K. Fujiwara,[58] Y. Fukao,[58] T. Fusayasu,[49] C. Gal,[65] P. Gallus,[15] P. Garg,[3] I. Garishvili,[39,66] H. Ge,[65] F. Giordano,[26] A. Glenn,[13,39] H. Gong,[65] M. Gonin,[37] Y. Goto,[58,59] R. Granier de Cassagnac,[37] N. Grau,[2,14] S. V. Greene,[69] M. Grosse Perdekamp,[26,59] T. Gunji,[12] H.-Å. Gustafsson,[42,*] T. Hachiya,[23,58] J. S. Haggerty,[7] K. I. Hahn,[19] H. Hamagaki,[12] J. Hamblen,[66] H. F. Hamilton,[1] R. Han,[56] S. Y. Han,[19] J. Hanks,[14,65] E. P. Hartouni,[39] S. Hasegawa,[30] T. O. S. Haseler,[22] K. Hashimoto,[58,60] E. Haslum,[42] R. Hayano,[12] X. He,[22] M. Heffner,[39] T. K. Hemmick,[65] T. Hester,[8] J. C. Hill,[29] M. Hohlmann,[20] R. S. Hollis,[8] W. Holzmann,[14] K. Homma,[23] B. Hong,[34] T. Horaguchi,[23] D. Hornback,[66] T. Hoshino,[23] N. Hotvedt,[29] J. Huang,[7] S. Huang,[69] T. Ichihara,[58,59] R. Ichimiya,[58] J. Ide,[47] Y. Ikeda,[68] K. Imai,[30,36,58] M. Inaba,[68] A. Iordanova,[8] D. Isenhower,[1] M. Ishihara,[58] T. Isobe,[12,58] M. Issah,[69] A. Isupov,[31] D. Ivanishchev,[57] B. V. Jacak,[65] M. Jezghani,[22] J. Jia,[7,64] X. Jiang,[40] J. Jin,[14] B. M. Johnson,[7] K. S. Joo,[48] D. Jouan,[55] D. S. Jumper,[1,26] F. Kajihara,[12] S. Kametani,[58] N. Kamihara,[59] J. Kamin,[65] S. Kanda,[12] J. H. Kang,[73] J. Kapustinsky,[40] K. Karatsu,[36,58] D. Kawall,[44,59] M. Kawashima,[58,60] A. V. Kazantsev,[35] T. Kempel,[29] J. A. Key,[51] V. Khachatryan,[65] A. Khanzadeev,[57] K. M. Kijima,[23] B. I. Kim,[34] C. Kim,[34] D. H. Kim,[48] D. J. Kim,[32] E. Kim,[63] E.-J. Kim,[10] G. W. Kim,[19] M. Kim,[63] S. H. Kim,[73] Y.-J. Kim,[26] B. Kimelman,[47] E. Kinney,[13] K. Kiriluk,[13] Á. Kiss,[18] E. Kistenev,[7] R. Kitamura,[12] J. Klatsky,[21] D. Kleinjan,[8] P. Kline,[65] T. Koblesky,[13] L. Kochenda,[57] B. Komkov,[57] M. Konno,[68] J. Koster,[26] D. Kotchetkov,[51,53] D. Kotov,[57,61] A. Kozlov,[71] A. Král,[15] A. Kravitz,[14] G. J. Kunde,[40] K. Kurita,[58,60] M. Kurosawa,[58,59] Y. Kwon,[73] G. S. Kyle,[52] R. Lacey,[64] Y. S. Lai,[14] J. G. Lajoie,[29] A. Lebedev,[29] D. M. Lee,[40] J. Lee,[19] K. Lee,[63] K. B. Lee,[34] K. S. Lee,[34] S Lee,[73] S. H. Lee,[65] M. J. Leitch,[40] M. A. L. Leite,[62] E. Leitner,[69] B. Lenzi,[62] X. Li,[11] P. Liebing,[59] S. H. Lim,[73] L. A. Linden Levy,[13] T. Liška,[15] A. Litvinenko,[31] H. Liu,[40,52] M. X. Liu,[40] B. Love,[69] R. Luechtenborg,[46] D. Lynch,[7] C. F. Maguire,[69] Y. I. Makdisi,[6] M. Makek,[74] A. Malakhov,[31] M. D. Malik,[51] A. Manion,[65] V. I. Manko,[35] E. Mannel,[7,14] Y. Mao,[56,58] H. Masui,[68] F. Matathias,[14] M. McCumber,[40,65] P. L. McGaughey,[40] D. McGlinchey,[13] C. McKinney,[26] N. Means,[65] A. Meles,[52] M. Mendoza,[8] B. Meredith,[26] Y. Miake,[68] A. C. Mignerey,[43] P. Mikeš,[9,28] K. Miki,[58,68] A. Milov,[7,71] D. K. Mishra,[4] M. Mishra,[3] J. T. Mitchell,[7] S. Miyasaka,[58,67] S. Mizuno,[58,68] A. K. Mohanty,[4] P. Montuenga,[26] T. Moon,[73] Y. Morino,[12] A. Morreale,[8] D. P. Morrison,[7,†] T. V. Moukhanova,[35] T. Murakami,[36,58] J. Murata,[58,60] A. Mwai,[64] S. Nagamiya,[33,58] K. Nagashima,[23] J. L. Nagle,[13,‡] M. Naglis,[71] M. I. Nagy,[18] I. Nakagawa,[58,59] H. Nakagomi,[58,68] Y. Nakamiya,[23] T. Nakamura,[33] K. Nakano,[58,67] C. Nattrass,[66] P. K. Netrakanti,[4] J. Newby,[39] M. Nguyen,[65] T. Niida,[68] S. Nishimura,[12] R. Nouicer,[7,59] T. Novak,[72] N. Novitzky,[32,65] A. S. Nyanin,[35] E. O'Brien,[7] S. X. Oda,[12] C. A. Ogilvie,[29] M. Oka,[68] K. Okada,[59] Y. Onuki,[58] J. D. Orjuela Koop,[13] J. D. Osborn,[45] A. Oskarsson,[42] M. Ouchida,[23,58] K. Ozawa,[12,33] R. Pak,[7] V. Pantuev,[27,65] V. Papavassiliou,[52] I. H. Park,[19] J. Park,[63] J. S. Park,[63] S. Park,[63] S. K. Park,[34] W. J. Park,[34] S. F. Pate,[52] M. Patel,[29] H. Pei,[29] J.-C. Peng,[26] H. Pereira,[16] D. V. Perepelitsa,[7] G. D. N. Perera,[52] V. Peresedov,[31] D. Yu. Peressounko,[35] J. Perry,[29] R. Petti,[7,65] C. Pinkenburg,[7] R. Pinson,[1] R. P. Pisani,[7] M. Proissl,[65] M. L. Purschke,[7] A. K. Purwar,[40] H. Qu,[22] J. Rak,[32] A. Rakotozafindrabe,[37] B. J. Ramson,[45] I. Ravinovich,[71] K. F. Read,[54,66] K. Reygers,[46] D. Reynolds,[64] V. Riabov,[50,57] Y. Riabov,[57,61] E. Richardson,[43] T. Rinn,[29] D. Roach,[69] G. Roche,[41,*] S. D. Rolnick,[8] M. Rosati,[29] C. A. Rosen,[13] S. S. E. Rosendahl,[42] P. Rosnet,[41] Z. Rowan,[5] J. G. Rubin,[45] P. Rukoyatkin,[31] P. Ružička,[28] B. Sahlmueller,[46,65] N. Saito,[33] T. Sakaguchi,[7] K. Sakashita,[58,67] H. Sako,[30] V. Samsonov,[50,57] S. Sano,[12,70] M. Sarsour,[22] S. Sato,[30,33] T. Sato,[68] S. Sawada,[33] B. Schaefer,[69] B. K. Schmoll,[66] K. Sedgwick,[8] J. Seele,[13] R. Seidl,[26,58,59] A. Yu. Semenov,[29] A. Sen,[66] R. Seto,[8] P. Sett,[4] A. Sexton,[43] D. Sharma,[65,71] I. Shein,[25] T.-A. Shibata,[58,67] K. Shigaki,[23] M. Shimomura,[29,68] K. Shoji,[36,58] P. Shukla,[4] A. Sickles,[7,26] C. L. Silva,[40,62] D. Silvermyr,[42,54] C. Silvestre,[16] K. S. Sim,[34] B. K. Singh,[3] C. P. Singh,[3] V. Singh,[3] M. Slunečka,[9] M. Snowball,[40] R. A. Soltz,[39] W. E. Sondheim,[40] S. P. Sorensen,[66] I. V. Sourikova,[7] N. A. Sparks,[1] P. W. Stankus,[54] E. Stenlund,[42] M. Stepanov,[44,52,*] S. P. Stoll,[7] T. Sugitate,[23] A. Sukhanov,[7] T. Sumita,[58] J. Sun,[65] J. Sziklai,[72] E. M. Takagui,[62] A. Taketani,[58,59] R. Tanabe,[68] Y. Tanaka,[49] K. Tanida,[36,58,59,63] M. J. Tannenbaum,[7] S. Tarafdar,[3,71] A. Taranenko,[50,64] P. Tarján,[17] H. Themann,[65] T. L. Thomas,[51] R. Tieulent,[22] A. Timilsina,[29] T. Todoroki,[58,68] M. Togawa,[36,58] A. Toia,[65] L. Tomášek,[28] M. Tomášek,[15,28] H. Torii,[23] C. L. Towell,[1] R. Towell,[1] R. S. Towell,[1] I. Tserruya,[71] Y. Tsuchimoto,[23] C. Vale,[7,29] H. Valle,[69] H. W. van Hecke,[40] E. Vazquez-Zambrano,[14] A. Veicht,[14,26] J. Velkovska,[69] R. Vértesi,[17,72]

A. A. Vinogradov,[35] M. Virius,[15] V. Vrba,[15,28] E. Vznuzdaev,[57] X. R. Wang,[52,59] D. Watanabe,[23] K. Watanabe,[68] Y. Watanabe,[58,59] Y. S. Watanabe,[12,33] F. Wei,[29,52] R. Wei,[64] J. Wessels,[46] A. S. White,[45] S. N. White,[7] D. Winter,[14] J. P. Wood,[1] C. L. Woody,[7] R. M. Wright,[1] M. Wysocki,[13,54] B. Xia,[53] W. Xie,[59] L. Xue,[22] S. Yalcin,[65] Y. L. Yamaguchi,[12,65] K. Yamaura,[23] R. Yang,[26] A. Yanovich,[25] J. Ying,[22] S. Yokkaichi,[58,59] J. H. Yoo,[34] I. Yoon,[63] Z. You,[56] G. R. Young,[54] I. Younus,[38,51] H. Yu,[56] I. E. Yushmanov,[35] W. A. Zajc,[14] A. Zelenski,[6] C. Zhang,[54] S. Zhou,[11] L. Zolin,[31] and L. Zou[8]

(PHENIX Collaboration)

[1]*Abilene Christian University, Abilene, Texas 79699, USA*

[2]*Department of Physics, Augustana University, Sioux Falls, South Dakota 57197, USA*

[3]*Department of Physics, Banaras Hindu University, Varanasi 221005, India*

[4]*Bhabha Atomic Research Centre, Bombay 400 085, India*

[5]*Baruch College, City University of New York, New York, New York 10010, USA*

[6]*Collider-Accelerator Department, Brookhaven National Laboratory, Upton, New York 11973-5000, USA*

[7]*Physics Department, Brookhaven National Laboratory, Upton, New York 11973-5000, USA*

[8]*University of California-Riverside, Riverside, California 92521, USA*

[9]*Charles University, Ovocný trh 5, Praha 1, 116 36 Prague, Czech Republic*

[10]*Chonbuk National University, Jeonju 561-756, Korea*

[11]*Science and Technology on Nuclear Data Laboratory, China Institute of Atomic Energy, Beijing 102413, People's Republic of China*

[12]*Center for Nuclear Study, Graduate School of Science, University of Tokyo, 7-3-1 Hongo, Bunkyo, Tokyo 113-0033, Japan*

[13]*University of Colorado, Boulder, Colorado 80309, USA*

[14]*Columbia University, New York, New York 10027, USA and Nevis Laboratories, Irvington, New York 10533, USA*

[15]*Czech Technical University, Zikova 4, 166 36 Prague 6, Czech Republic*

[16]*Dapnia, CEA Saclay, F-91191 Gif-sur-Yvette, France*

[17]*Debrecen University, Egyetem tér 1, H-4010 Debrecen, Hungary*

[18]*ELTE, Eötvös Loránd University, Pázmány P. s. 1/A, H-1117 Budapest, Hungary*

[19]*Ewha Womans University, Seoul 120-750, Korea*

[20]*Florida Institute of Technology, Melbourne, Florida 32901, USA*

[21]*Florida State University, Tallahassee, Florida 32306, USA*

[22]*Georgia State University, Atlanta, Georgia 30303, USA*

[23]*Hiroshima University, Kagamiyama, Higashi-Hiroshima 739-8526, Japan*

[24]*Department of Physics and Astronomy, Howard University, Washington, DC 20059, USA*

[25]*IHEP Protvino, State Research Center of Russian Federation, Institute for High Energy Physics, Protvino 142281, Russia*

[26]*University of Illinois at Urbana-Champaign, Urbana, Illinois 61801, USA*

[27]*Institute for Nuclear Research of the Russian Academy of Sciences, prospekt 60-letiya Oktyabrya 7a, Moscow 117312, Russia*

[28]*Institute of Physics, Academy of Sciences of the Czech Republic, Na Slovance 2, 182 21 Prague 8, Czech Republic*

[29]*Iowa State University, Ames, Iowa 50011, USA*

[30]*Advanced Science Research Center, Japan Atomic Energy Agency, 2-4 Shirakata Shirane, Tokai-mura, Naka-gun, Ibaraki-ken 319-1195, Japan*

[31]*Joint Institute for Nuclear Research, 141980 Dubna, Moscow Region, Russia*

[32]*Helsinki Institute of Physics and University of Jyväskylä, P.O. Box 35, FI-40014 Jyväskylä, Finland*

[33]*KEK, High Energy Accelerator Research Organization, Tsukuba, Ibaraki 305-0801, Japan*

[34]*Korea University, Seoul 136-701, Korea*

[35]*Russian Research Center "Kurchatov Institute," Moscow 123098, Russia*

[36]*Kyoto University, Kyoto 606-8502, Japan*

[37]*Laboratoire Leprince-Ringuet, Ecole Polytechnique, CNRS-IN2P3, Route de Saclay, F-91128 Palaiseau, France*

[38]*Physics Department, Lahore University of Management Sciences, Lahore 54792, Pakistan*

[39]*Lawrence Livermore National Laboratory, Livermore, California 94550, USA*

[40]*Los Alamos National Laboratory, Los Alamos, New Mexico 87545, USA*

[41]*LPC, Université Blaise Pascal, CNRS-IN2P3, Clermont-Fd, 63177 Aubiere Cedex, France*

[42]*Department of Physics, Lund University, Box 118, SE-221 00 Lund, Sweden*

[43]*University of Maryland, College Park, Maryland 20742, USA*

[44]*Department of Physics, University of Massachusetts, Amherst, Massachusetts 01003-9337, USA*

[45]*Department of Physics, University of Michigan, Ann Arbor, Michigan 48109-1040, USA*

[46]*Institut für Kernphysik, University of Muenster, D-48149 Muenster, Germany*

[47]*Muhlenberg College, Allentown, Pennsylvania 18104-5586, USA*

[48]*Myongji University, Yongin, Kyonggido 449-728, Korea*

[49]*Nagasaki Institute of Applied Science, Nagasaki-shi, Nagasaki 851-0193, Japan*

[50]*National Research Nuclear University, MEPhI, Moscow Engineering Physics Institute, Moscow 115409, Russia*

[51]*University of New Mexico, Albuquerque, New Mexico 87131, USA*

[52]*New Mexico State University, Las Cruces, New Mexico 88003, USA*
[53]*Department of Physics and Astronomy, Ohio University, Athens, Ohio 45701, USA*
[54]*Oak Ridge National Laboratory, Oak Ridge, Tennessee 37831, USA*
[55]*IPN-Orsay, Universite Paris Sud, CNRS-IN2P3, BP1, F-91406 Orsay, France*
[56]*Peking University, Beijing 100871, People's Republic of China*
[57]*PNPI, Petersburg Nuclear Physics Institute, Gatchina, Leningrad Region 188300, Russia*
[58]*RIKEN Nishina Center for Accelerator-Based Science, Wako, Saitama 351-0198, Japan*
[59]*RIKEN BNL Research Center, Brookhaven National Laboratory, Upton, New York 11973-5000, USA*
[60]*Physics Department, Rikkyo University, 3-34-1 Nishi-Ikebukuro, Toshima, Tokyo 171-8501, Japan*
[61]*Saint Petersburg State Polytechnic University, St. Petersburg 195251 Russia*
[62]*Universidade de São Paulo, Instituto de Física, Caixa Postal 66318, São Paulo CEP05315-970, Brazil*
[63]*Department of Physics and Astronomy, Seoul National University, Seoul 151-742, Korea*
[64]*Chemistry Department, Stony Brook University, SUNY, Stony Brook, New York 11794-3400, USA*
[65]*Department of Physics and Astronomy, Stony Brook University, SUNY, Stony Brook, New York 11794-3800, USA*
[66]*University of Tennessee, Knoxville, Tennessee 37996, USA*
[67]*Department of Physics, Tokyo Institute of Technology, Oh-okayama, Meguro, Tokyo 152-8551, Japan*
[68]*Center for Integrated Research in Fundamental Science and Engineering, University of Tsukuba, Tsukuba, Ibaraki 305, Japan*
[69]*Vanderbilt University, Nashville, Tennessee 37235, USA*
[70]*Waseda University, Advanced Research Institute for Science and Engineering, 17 Kikui-cho, Shinjuku-ku, Tokyo 162-0044, Japan*
[71]*Weizmann Institute, Rehovot 76100, Israel*
[72]*Institute for Particle and Nuclear Physics, Wigner Research Centre for Physics, Hungarian Academy of Sciences (Wigner RCP, RMKI), PO Box 49, H-1525 Budapest 114, Hungary*
[73]*Yonsei University, IPAP, Seoul 120-749, Korea*
[74]*University of Zagreb, Faculty of Science, Department of Physics, Bijenička 32, HR-10002 Zagreb, Croatia*
(Received 21 April 2015; published 23 September 2015)

We present a systematic study of charged-pion and kaon interferometry in Au + Au collisions at $\sqrt{s_{NN}} =$ 200 GeV. The kaon mean source radii are found to be larger than pion radii in the outward and longitudinal directions for the same transverse mass; this difference increases for more central collisions. The azimuthal-angle dependence of the radii was measured with respect to the second-order event plane and similar oscillations of the source radii were found for pions and kaons. Hydrodynamic models qualitatively describe the similar oscillations of the mean source radii for pions and kaons, but they do not fully describe the transverse-mass dependence of the oscillations.

DOI: 10.1103/PhysRevC.92.034914 PACS number(s): 25.75.Dw

I. INTRODUCTION

Measurements of the quark-gluon plasma (QGP) produced in nucleus-nucleus collisions at the Relativistic Heavy Ion Collider (RHIC) [1–4] and the Large Hadron Collider (LHC) [5–7] showed that the QGP exhibits rapid hydrodynamic expansion, followed by hadronization, which results in the emission of many particles. The time of last scattering among hadrons is referred to as kinetic freeze-out. To understand the dynamics and properties of the QGP, it is important to understand the full system evolution and how it is constrained by the measurements of the space-time distribution at kinetic freeze-out.

The quantum statistical interferometry of identical particles, also known as Hanbury-Brown–Twiss (HBT) interferometry or femtoscopy, is a powerful tool to measure the spatial and temporal scales of systems created in nucleus-nucleus collisions [8,9]. This technique was first developed to measure the angular diameter of stars through intensity interferometry of radio waves [10]. It has also been applied to nuclear and particle physics [11]. In nucleus-nucleus collisions, the interferometry using emitted hadrons measures the spatial extent of the particle-emitting source at the time of kinetic freeze-out.

Despite the successful description of various observables at RHIC by the hydrodynamic models [1,2], there was significant discrepancy between HBT data and theoretical models [2,12]. Recent theoretical development has improved the agreement by including realistic physics conditions such as a stiffer equation of state and a viscosity of the created matter [13].

Charged pions are often used for the interferometry analysis because of their abundant production, but recently acquired large data sets by RHIC and LHC experiments allow study of the particle-species dependence [14–16]. Kaon interferometry is of particular interest because the contribution from resonance decays is reduced compared to that seen

*Deceased.
†PHENIX Cospokesperson: morrison@bnl.gov
‡PHENIX Cospokesperson: jamie.nagle@colorado.edu

with pions [17,18], thereby providing a more direct view of the particle-emitting source. PHENIX at RHIC published an analysis of one-dimensional source imaging for charged kaons [14]. STAR at RHIC has recently published three-dimensional source imaging [15], where charged kaons lack the non-Gaussian tail in the source function observed in the pion sample. This result may be caused by the reduced contribution from long-lived resonances, as well as a different time dependence owing to a shorter rescattering phase. Further systematic studies using different particle species are needed to better constrain the space-time evolution and freeze-out distributions of the created medium.

The HBT measurement is also sensitive to the initial spatial anisotropy and the subsequent evolution of the created matter. Owing to the strong collective expansion, one might expect the eccentricity of the source shape in the initial state to be reduced at freeze-out and possibly to be reversed if the collective expansion is stronger in the direction of the reaction plane or if the expansion time is sufficiently long. To probe the spatial source anisotropy at freeze-out, HBT measurements with respect to the event planes have been performed using two-pion correlation [19–22]. Large oscillations of the pion source radii relative to the second-order event plane were observed, which indicates that the pion source at freeze-out is elongated in the direction perpendicular to the event plane even after the collective expansion.

In this paper, we present azimuthal-integrated and azimuthal-dependent source radii for charged pions and kaons in Au + Au collisions at $\sqrt{s_{NN}} = 200$ GeV. Results are compared with the hydrodynamic models for both particle species.

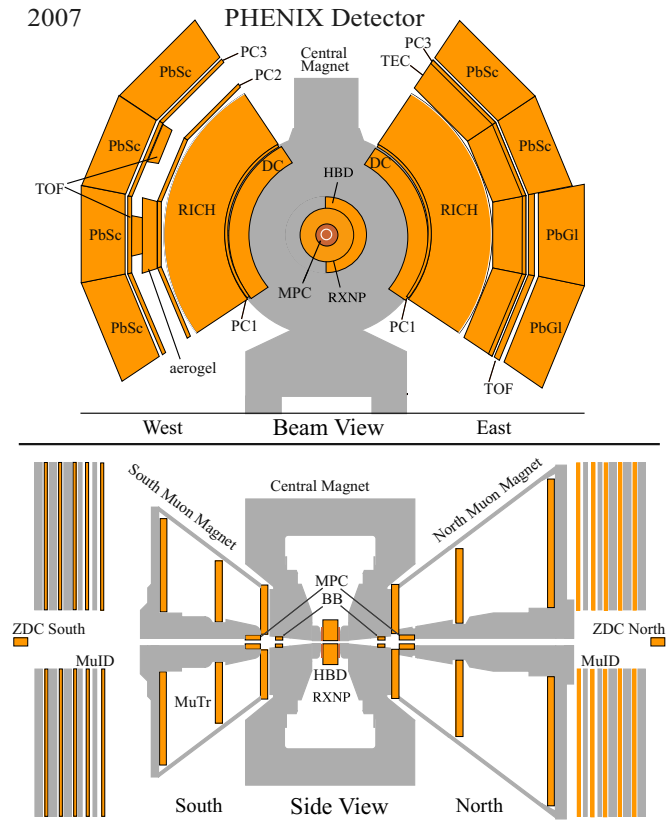

FIG. 1. (Color online) The layout of PHENIX detectors in the 2007 run configuration. The top figure shows the central arm detectors viewed along the beam axis. The bottom figure shows the side view of the global detectors and muon arm detectors.

II. EXPERIMENT

The PHENIX experiment [23] is designed to measure particles produced in nucleus-nucleus collisions with good momentum resolution, including photons, electrons, muons, and hadrons, to study properties of the QGP. The PHENIX detectors are composed of magnet systems and detectors for particle tracking and identification, event timing, plus vertex position and centrality determination. The particle tracking and identification detectors are arranged into central and forward (muon) arms. Figure 1 shows the layout of the PHENIX detector during the 2007 running period.

Global detectors characterize the global event characteristics in heavy-ion collisions. The beam-beam counters (BBCs) [24] measure the collision time and the position of the collision vertex along the beam axis, as well as the collision centrality. The BBC comprises two identical sets of counters located ±144 cm from the nominal collision point and surrounds the beam pipe covering the pseudorapidity range of $3.0 < |\eta| < 3.9$. Each BBC has 64 modules of Čerenkov radiators and measures the number of charged particles in its acceptance. The zero-degree calorimeters are located 18 m from the nominal collision point and measure the energy of spectator neutrons. The reaction-plane detector (RXNP) [25] was installed prior to the 2007 RHIC run to measure the event-plane angle in heavy-ion collisions. The RXNP comprises two sets of 24 scintillators on both the north and the south sides and is located ±39 cm from the vertex position. The scintillators are arranged around the beam pipe in two concentric rings of 12 segments in the azimuthal direction. The outer and inner rings cover pseudorapidity ranges of $1.0 < |\eta| < 1.5$ and $1.5 < |\eta| < 2.8$, respectively.

The PHENIX central arms comprise two sets of detectors located on the west and east sides of the beam axis. Each arm covers 90° in azimuth and a pseudorapidity range of $|\eta| < 0.35$. Track and momentum reconstructions of charged particles were performed with the drift chambers (DCs) and pad chambers (PCs). The DCs are located at a radial distance of 2.02 to 2.46 m from the beam axis in the west and east arms, covering 2 m length along the beam axis. The PCs are multiwire proportional chambers in each of the central arms and are located at radial distances of 2.5 m (PC1) and 4.9 m (PC3). The tracks and momenta were reconstructed by combining the hit information in the DC and PC1, providing a momentum resolution of $\delta p/p \approx 1.3\% \oplus 1.2\% \times p$ GeV/c [26]. Global-track reconstruction was performed by associating these tracks with hits in the outer detectors, such as PC3 and the lead-scintillator (PbSc) electromagnetic calorimeters, as shown in Fig. 1. Particle identification is provided by the PbSc [27], which is a sampling calorimeter with a timing resolution of about 500 ps [26] located at a radial distance of 5.1 m from the beam axis.

III. DATA ANALYSIS

The $\sqrt{s_{NN}} = 200$-GeV Au + Au collision data were collected by PHENIX during the 2007 running period. A total of 4.2×10^9 events were used for this analysis, where the minimum bias trigger with at least two hits in each BBC was required. This trigger measures $92 \pm 3\%$ of the total inelastic cross section [28]. Additional off-line requirements of one zero-degree-calorimeter hit on each side and a collision vertex position of less than ± 30 cm were applied.

A. Track selection

Charged tracks with good quality were selected based on the track information from the DC and PC1. To reduce the background owing to the random association of hits and reconstructed tracks, track residuals were required to be less than 2σ in the $\phi - z$ plane at the PC3 and PbSc for pions. For kaons, this cut was relaxed to 2.5σ to increase statistics. The fraction of the random background is ~4.6% after the 2σ cuts and ~5.3% after the 2.5σ cuts at $p_T = 0.5$ GeV/c in the 0%–10% most central collisions. The effect of the track quality cuts was included in the systematic uncertainty.

B. Particle identification

Particle identification was performed by combining time-of-flight data from the PbSc in the west arm, the reconstructed momentum, and flight path length from the collision vertex to the hit position at the PbSc wall. The squared mass of the particles is given by the formula

$$m^2 = \frac{p^2}{c^2}\left[\left(\frac{ct}{L}\right)^2 - 1\right], \tag{1}$$

where p is the momentum, t is the time of flight, L is the flight path length, and c is the speed of light. Pions and kaons were selected from a 2σ window around their peaks in the squared mass distribution. Additional requirements, i.e., to be away from the mass peak of other particles, were applied to reduce contamination. The π/K separation was achieved up to a momentum of ~1 GeV/c. Contamination in the pion samples from kaons is below 1% for $p \approx 1$ GeV/c and contamination in the kaon samples from pions (protons) is below 4% (1%) for $p \approx 1$ GeV/c.

C. Construction of the correlation function

In this section, a bold character denotes four-dimensional vector and an arrow denotes three-dimensional vector.

The experimental correlation function defined as

$$C_2(\mathbf{q}) = \frac{A(\mathbf{q})}{B(\mathbf{q})} \tag{2}$$

was measured as a function of the pair momentum difference $\mathbf{q} = \mathbf{p_1} - \mathbf{p_2}$, where A and B are constructed from identical particle pairs from the same event and a mixed event, respectively. The mixed events are taken from similar event centralities and vertex positions. In the case of azimuthal-dependent analysis, the mixed events are also required to have similar values for the second-order event plane defined in Sec. III D.

Particle pairs with similar momenta and spatially close to each other are affected by incorrect track reconstruction and detector inefficiencies. These effects were removed by applying pair selection cuts at the DC and PbSc following our previous analysis [14,22]. In addition, pairs that are associated with hits on the same tower of the PbSc were removed.

The particle pairs were analyzed with the Bertsch-Pratt parametrization [29,30] as functions of the pair momentum difference $\mathbf{q}$ and mean pair momentum $\vec{k}$, where $\vec{k} = (\vec{p}_1 + \vec{p}_2)/2$. The $\vec{k}$ is projected into its longitudinal component k_z and transverse component $\vec{k}_T$. The $\mathbf{q}$ is projected into the longitudinal (q_l), outward (q_o), and sidewards (q_s) components, where q_l denotes the beam direction, q_o is perpendicular to $\vec{k}_T$, and q_s is perpendicular to both q_l and q_o. In this frame, the energy (temporal) component of the four-dimensional vector is taken in the outward component by performing the analysis in the longitudinal comoving system, where $k_z = 0$.

The $C_2(\mathbf{q})$ function is divided into two components based on the core-halo picture in which the λ parameter controls the relative strength of the core and the halo,

$$\begin{aligned} C_2(\mathbf{q}) &= C_2^{\text{core}} + C_2^{\text{halo}} \\ &= \lambda[1 + G(\mathbf{q})]F_c(q) + (1 - \lambda), \end{aligned} \tag{3}$$

$$G(q_s, q_o, q_l) = e^{-R_s^2 q_s^2 - R_o^2 q_o^2 - R_l^2 q_l^2 - 2R_{os}^2 q_s q_o}. \tag{4}$$

The $F_c(q)$ is the Coulomb correction factor evaluated by the Coulomb wave function [31,32], where q is the scalar quantity of $\mathbf{q}$. The central core contributes to the quantum statistical interference. The halo includes the decay of long-lived particles for which the quantum statistical interference occurs in a q range that is too small to be resolved experimentally and for which the Coulomb interaction is negligible. The core is assumed to be a Gaussian source as given by Eq. (4).

The HBT radii denoted by R_s, R_o, and R_l represent the spatial extent of the emission region in each direction, but R_o and to a lesser extent R_l and R_{os} include a contribution from the emission duration. All radii are sensitive to position-momentum correlations. The R_{os} term arises in the case of azimuthal-dependent analysis owing to asymmetries in the emission region [9], while it vanishes in the azimuthal-integrated analysis.

The HBT radii were measured as a function of k_T and presented as a function of the transverse mass $m_T = (k_T^2 + m^2)^{1/2}$ to study particle-species dependence, where m is the particle mass.

D. Event-plane dependence

The second-order event-plane angle (Ψ_2) was determined using the RXNP detector based on the azimuthal anisotropy of emitted particles in momentum space,

$$\Psi_2 = \frac{1}{2}\tan^{-1}\left(\frac{Q_y}{Q_x}\right), \tag{5}$$

$$Q_x = \sum w_i \cos(2\phi_i), \tag{6}$$

$$Q_y = \sum w_i \sin(2\phi_i), \tag{7}$$

where ϕ_i is the azimuthal angle of each segment i in the RXNP and w_i is the weight which reflects the particle multiplicity in that segment. Corrections for detector acceptance as detailed in Ref. [33] were applied.

Owing to the finite number of particles within the RXNP acceptance, the observed event plane Ψ_2 is smeared around the true event plane Φ. This smearing effect is typically accounted for by the resolution. The event-plane resolution defined as $\mathrm{Res}\{\Psi_2\} = \langle\cos[2(\Psi_2 - \Phi)]\rangle$ was estimated by the two-subevent method [34] using the event-plane correlation between the RXNP at forward and backward angles. The $\mathrm{Res}\{\Psi_2\}$ has a maximum of 0.75 in midcentral events [26].

The finite event-plane resolution reduces the oscillation amplitude of HBT radii relative to the event plane. To take this effect into account, a model-independent correction suggested in Ref. [35] was applied. The pair distribution measured at a certain azimuthal angle ϕ relative to the reconstructed event plane, $N(\mathbf{q},\phi - \Psi_2)$, is smeared by the finite event-plane resolution and finite width of angular bins Δ. The Fourier coefficients for the true and measured $N(\mathbf{q},\phi - \Psi_2)$, $N_{\alpha,n}(\mathbf{q},\phi - \Psi_2)$, can be associated with the relation

$$N^{\mathrm{exp}}_{\alpha,n}(\mathbf{q},\phi - \Psi_2) = N^{\mathrm{true}}_{\alpha,n}(\mathbf{q},\phi - \Phi)\frac{\sin(n\Delta/2)}{n\Delta/2}\langle\cos[n(\Psi_2 - \Phi)]\rangle, \quad (8)$$

where α denotes sine and cosine terms of the Fourier coefficients ($\alpha = s,c$) and n denotes the order of the coefficient. The above equation is analogous to the correction for the elliptic flow (v_2). Based on Eq. (9), the $A(\mathbf{q})$ and $B(\mathbf{q})$ functions can be unfolded by using the equation

$$N(q,\phi_j) = N_{\mathrm{exp}}(q,\phi_j) + 2\sum_{n=m,2m,\cdots}^{n_{\mathrm{bin}}/2}\zeta_{n,m}(\Delta) \times\left[N^{\mathrm{exp}}_{c,n}(q)\cos(n\phi_j) + N^{\mathrm{exp}}_{s,n}(q)\sin(n\phi_j)\right], \quad (9)$$

where n_{bin} is the number of azimuthal angular bins, and m is the order of the event plane, and ϕ_j denotes the center of the jth angular bin which corresponds to the azimuthal angle of the pair with respect to the event plane. $N^{\mathrm{exp}}_{c,n}(q)$, $N^{\mathrm{exp}}_{s,n}(q)$, and $\zeta_{n,m}(\Delta)$ are given by

$$N^{\mathrm{exp}}_{c,n}(q) = \langle N_{\mathrm{exp}}(q,\phi - \Psi_2)\cos[n(\phi - \Psi_2)]\rangle, = \sum_j N_{\mathrm{exp}}(q,\phi_j)\cos(n\phi_j)/n_{\mathrm{bin}}, \quad (10)$$

$$N^{\mathrm{exp}}_{s,n}(q) = \langle N_{\mathrm{exp}}(q,\phi - \Psi_2)\sin[n(\phi - \Psi_2)]\rangle, = \sum_j N_{\mathrm{exp}}(q,\phi_j)\sin(n\phi_j)/n_{\mathrm{bin}}, \quad (11)$$

$$\zeta_{n,m}(\Delta) = \frac{n\Delta/2}{\sin(n\Delta/2)\left\langle\cos\left[n\left(\Psi^{\mathrm{obs}}_m - \Phi\right)\right]\right\rangle} - 1. \quad (12)$$

The details of Eqs. (9)–(12) can be found in Ref. [35].

E. Systematic uncertainties

Systematic uncertainties were estimated by variations of track quality cuts at PC3 and PbSc, pair selection cuts, and particle identification (PID) cuts. Also, the effect of the Coulomb correction was studied by varying the input source size in the calculation of $F_c(q)$ in Eq. (3). Typical systematic uncertainties of the measured radii for charged pions and kaons are listed in Tables I and II.

TABLE I. Typical systematic uncertainties of HBT parameters for positive pion pairs in 0%–10% centrality and $0.6 < k_T < 0.7$ GeV/c.

Systematic source	λ	R_{s} (%)	R_{o} (%)	R_{l} (%)
Track quality	1.8	0.3	0.5	3.1
Pair selection	4.3	1.0	4.6	3.7
Particle ID	0.4	0.3	1.3	0.0
Coulomb	0.4	0.1	0.3	0.1
Total	4.7	1.1	4.8	4.8

In the azimuthal-dependent analysis, the variations when using different event planes from forward, backward, and both combined RXNPs were also incorporated. The systematic uncertainties of the oscillation amplitudes of HBT radii were dominated by the event-plane determination, which were 16%, on average, in the final eccentricity defined by the oscillation of R^2_{s} and the same fraction of the uncertainty was assumed for pions and kaons.

The effect of momentum resolution was studied employing the same method as previous analyses [36,37]. The momentum was smeared according to the known momentum resolution and the correlation function was reconstructed using the smeared $A(\mathbf{q})$ and $B(\mathbf{q})$ functions. By taking the ratio of the smeared and unsmeared correlation function, the correction factor was obtained. The correction on the momentum resolution was performed by multiplying the correction factor to the measured correlation function. The correction did not affect R_{s} and R_{l}, but slightly increased λ (<10%) and R_{o} (<6%).

IV. RESULTS AND DISCUSSION

A. Azimuthal-integrated analysis

Figures 2(a)–2(c) show an example of correlation functions of pion pairs and kaon pairs in 0%–10% centrality in a k_T bin with fit lines given by Eq. (3), where the momentum correction is not applied. The k_T range is selected to have similar m_T for pions and kaons. The three-dimensional $A(\mathbf{q})$ and $B(\mathbf{q})$ functions are projected in each $\mathbf{q}$ direction. In the projection, the other q are restricted to be less than 40 MeV/c [e.g., when

TABLE II. Typical systematic uncertainties of HBT parameters for charge-combined kaon pairs in 0%–10% centrality and $0.3 < k_T < 0.68$ GeV/c.

Systematic source	λ	R_{s} (%)	R_{o} (%)	R_{l} (%)
Track quality	5.1	2.2	1.9	2.2
Pair selection	9.0	1.5	0.1	1.9
Particle ID	6.1	0.3	4.5	0.1
Coulomb	4.6	0.3	1.1	0.2
Total	12.9	2.7	5.0	2.9

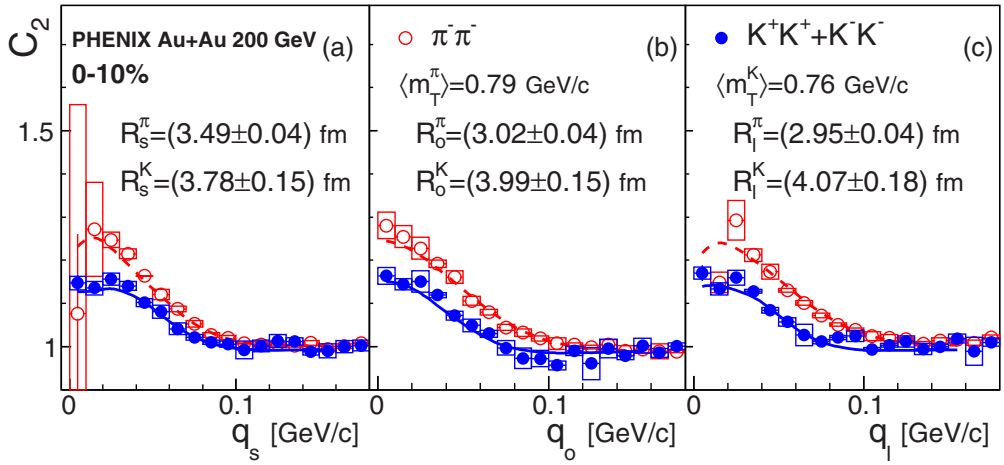

FIG. 2. (Color online) Correlation functions of negative pions and charged kaons for 0%–10% centrality (a)–(c), where positive and negative kaons are combined. Open boxes show the systematic uncertainties. Solid and dashed lines show the fit functions and the extracted radii values are shown in the figure.

making $C_2(q_s)$, the projection ranges of q_o and q_l should be $q_o < 40$ MeV and $q_l < 40$ MeV]. The 1D correlation functions shown in Fig. 2 are obtained by taking the ratio of the projected $A(\mathbf{q})$ and $B(\mathbf{q})$ functions. The extracted HBT radii with the statistical uncertainties are also shown in each panel. The width of the enhancement at the low $\mathbf{q}$ region in the correlation function is proportional to the inverse of the HBT radius. The width of the correlation function is comparable between pions

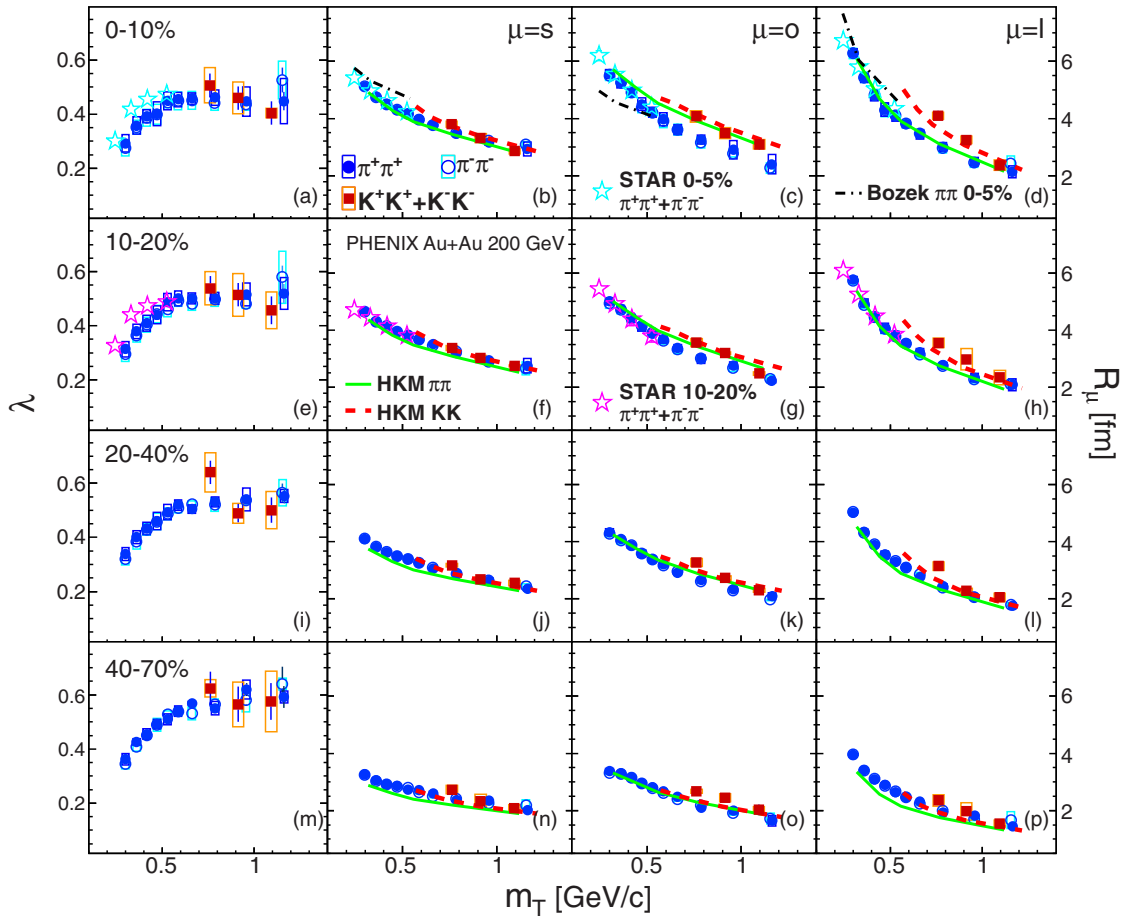

FIG. 3. (Color online) Extracted HBT parameters of charged pions and kaons as a function of m_T for the centralities indicated, where open boxes show the systematic uncertainties. Results of charged pions from STAR [37] are compared. Calculations from the hydrokinetic model (HKM) [38] and viscous-hydrodynamic model (Bozek) [39] are also shown.

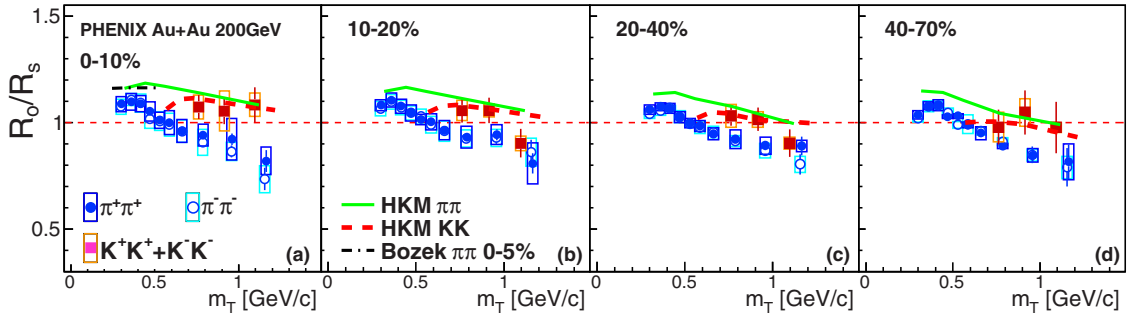

FIG. 4. (Color online) Ratio of R_o and R_s for charged pions and kaons as a function of m_T. Calculations from the hydrokinetic model (HKM) [38] and viscous-hydrodynamic model (Bozek) [39] are also shown.

and kaons in the sidewards direction, but narrower for kaons in the outward and longitudinal directions, indicating a larger radius in those directions than for pions with a similar mean m_T. We note that the data points at lower q bins fluctuate owing to lower statistics. The effect of the fluctuation on the radii was studied by varying the fit range and it was found to be within a few percent for both pions and kaons.

Figure 3 shows the extracted HBT parameters of charged pions and kaons for four centrality classes as a function of m_T. Results for charged pions in the low-m_T region from STAR [37] are also plotted. The source parameters from the two experiments are in good agreement, but the λ parameters are 20% lower at low m_T. The value of λ is sensitive to the combinatorial background level, which may differ between PHENIX and STAR. Positive and negative pions are quite consistent. The presented data are also consistent with our previous results [12,14].

The decrease of HBT radii with m_T is often attributed to the position-momentum correlation induced by collective flow. The slope of the m_T dependence becomes steeper for more central collisions, which is consistent with an expectation of a stronger radial flow [9]. R_s shows approximate m_T scaling between pions and kaons, as predicted by the Buda-Lund model [40], which is based on the analytic approach of the perfect fluid hydrodynamics. However, R_o and R_l of kaons show larger values than those of pions as noted already in Fig. 2, where the m_T scaling is broken. The difference increases with centrality going from peripheral to central collisions. The similar difference between pions and kaons for R_l was reported by STAR [15].

The results are compared with the HKM [38,41]. The HKM incorporates realistic conditions such as the Glauber initial condition, crossover transition, fluid hydrodynamics, microscopic transport, and resonance decays, but does not explicitly include the viscous correction. It is reported that the model calculations with the initial condition of the color glass condensate are very similar to those with the Glauber initial condition [41]. As shown in Fig. 3, the HKM [38] describes well the overall trend of HBT radii for pions and kaons in all centrality bins; however, it overestimates R_o of pions in more central collisions and underestimates R_s and R_l of pions in peripheral collisions. The HKM also describes the difference of pions and kaons in the longitudinal direction, which can be understood by strong transverse flow [42], but the difference in the outward direction cannot be explained well. The data for pions in most central collisions are also compared with (3 + 1)-D viscous hydrodynamic model [39] calculations which employ a Glauber initial condition and $\eta/s = 0.08$ (also see Sec. IV B 3 for details). The model follows the general trends in the data.

The ratio of R_o and R_s, which is sensitive to the emission duration of particles, is also plotted as a function of m_T in Fig. 4. Results for both species do not show any significant centrality dependence, but the values for kaons are larger than those for pions at all m_T and centralities, a possible indication of longer emission duration time for kaons than for pions.

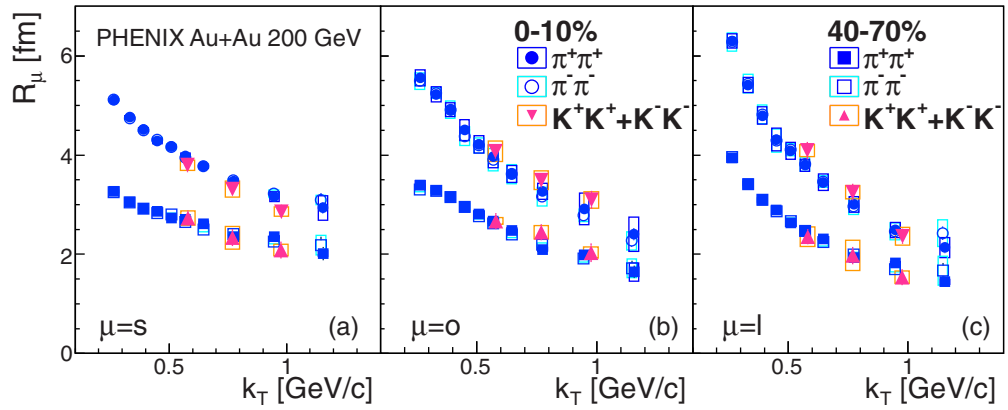

FIG. 5. (Color online) HBT radii of charged pions and kaons as a function of k_T, where open boxes show the systematic uncertainties.

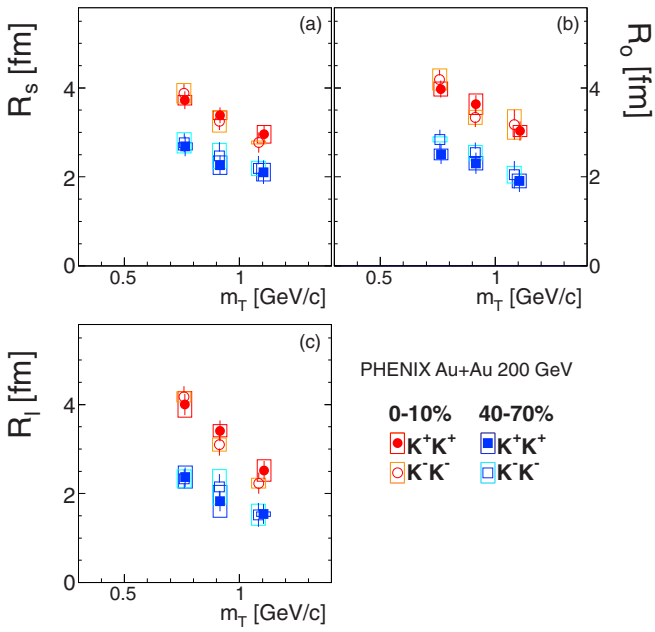

FIG. 6. (Color online) Comparison of HBT radii between positive and negative kaons pairs in central and peripheral collisions, where open boxes show the systematic uncertainties.

The HKM reproduces the data for kaons well, but not for pions.

The m_T scaling of HBT radii was inspired by the hydrodynamic expansion [43]. This is based on the idea that the kinetic freeze-out of hadrons occurs at the same time and the hadrons with similar velocities are emitted from the same homogeneity region. In other words, the homogeneity length depends on the particle mass under the presence of radial flow. In Fig. 5, both pion and kaon HBT radii for central and peripheral events are plotted as functions of k_T. Unlike the case of the m_T dependence shown in Fig. 3, both radii seem to be scaled better for k_T in all q directions as predicted in Ref. [42]. This model includes many different effects such as the hadronic cascade and resonance decays in addition to radial flow.

We have also checked charge-dependent kaon HBT radii in Fig. 6. There was no significant difference between positive and negative kaons, as we expected. If nucleons are dominant in the particle-emitting source and the net baryon density is not small, the measured radii might be different between K^+ and K^- (and also pions) because of smaller cross section of $K^+ - N$ than $K^- - N$ [44]. However, this is not observed.

B. Azimuthal-dependent analysis

1. Results

We have measured the azimuthal angle dependence of HBT radii with respect to Ψ_2 for both charged pions and kaons. Figures 7(a)–7(c) show the correlation functions of charged kaons in the 20%–60% centrality bin in the in-plane ($|\phi - \Psi_2| < \pi/16$) and out-of-plane ($|\phi - \Psi_2 - \pi/2| < \pi/16$) directions without correction for the event-plane resolution. The correlation functions in Fig. 7 are calculated in the same way as Fig. 2, i.e., when making the one-dimensional C_2 along the q of interest, the other q are limited to be less than 50 MeV/c. To make a comparison of the C_2 width between in-plane and out-of-plane directions, the C_2 in the positive and negative q are averaged because they are symmetric over $q = 0$ within the statistical uncertainties. The extracted radii without the correction are also shown in the figure. A difference of the width in the correlation function between these (in and out-of-plane) directions can be seen in the sidewards [Fig. 7(a)] direction. Figure 8 shows the extracted HBT radii of charged kaons as a function of azimuthal pair angle ϕ with respect to Ψ_2 for two centrality bins where $\langle k_T \rangle$ is ~0.77 GeV/c. We first fix λ in Eq. (3) by taking the average for λ obtained in all azimuthal bins, then we fit in individual azimuthal bins again with fixed λ parameter as detailed in Ref. [37]. This treatment is based on the assumption that λ has no azimuthal angle dependence, and the data fluctuate but do not depend on the azimuthal angle beyond the systematic uncertainty. The cosine

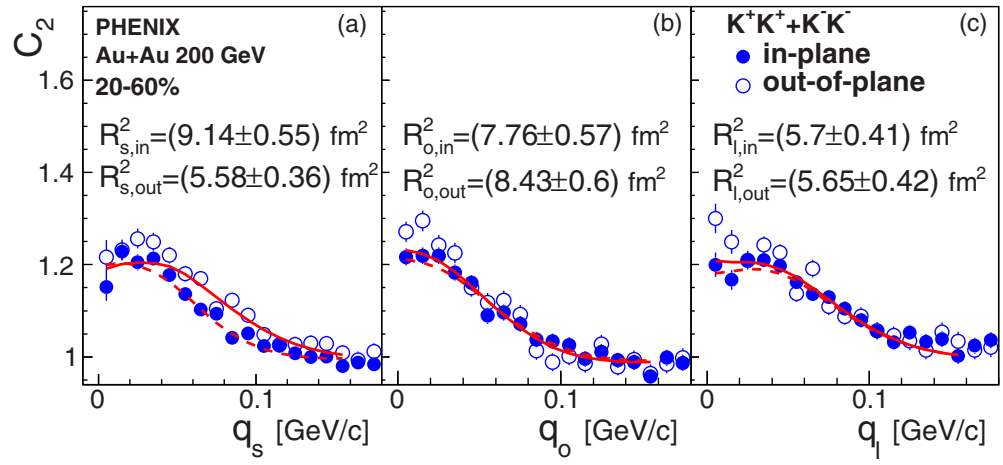

FIG. 7. (Color online) Correlation functions of charged kaons in 20%–60% centrality (a)–(c), where positive and negative kaons are combined. The correlation functions along q_s and q_o directions are averaged out between positive and negative q. Lines show the fit functions and the extracted radii values are shown in the figure.

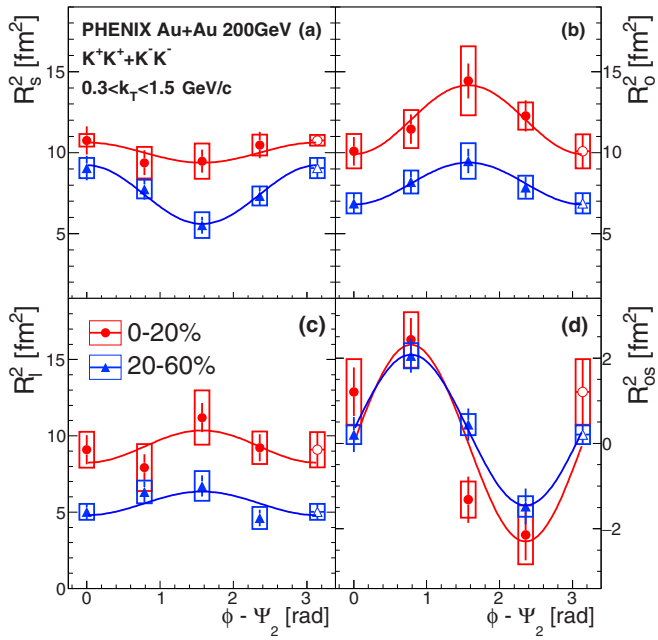

FIG. 8. (Color online) Squared HBT radii of charged kaon pairs as a function of azimuthal pair angle ϕ with respect to Ψ_2 for two centrality bins, where k_T is integrated over 0.3–1.5 GeV/c. The open symbols at $\phi - \Psi_2 = \pi$ are the same data as that at $\phi - \Psi_2 = 0$. Open boxes show systematic uncertainties and the solid lines are the fitting functions given by Eq. (13).

oscillations of R_s^2 and R_o^2 [Figs. 8(a) and 8(b)] and the sine oscillation of R_{os}^2 [Fig. 8(d)] can be clearly seen. Nonzero R_{os} at $(\phi - \Psi_2) = \frac{1}{4}\pi, \frac{3}{4}\pi$ implies that the direction of the particle emission is tilted relative to the main axis of the emission region. The oscillation of R_s^2 seems to be larger than for R_o^2 in 20%–60% centrality bin.

We have also measured the charged-pion HBT radii with respect to Ψ_2 for the same centrality bins as kaons with six k_T (m_T) bins, as shown in Fig. 9. The averages of R_s^2, R_o^2, and R_l^2 decrease with k_T, as seen in Fig. 3. The R_s^2 and R_o^2 have similar but opposite oscillations in all k_T bins. For 20%–60% centrality, both transverse radii show finite oscillation even in the lowest k_T bin, which indicates that the pion emission happens from an elliptical source. For 0%–20% centrality, the R_s^2 has a weak azimuthal angle dependence, while the R_o^2 has a larger oscillation than the R_s^2. It could be consistent with R_o^2 being more influenced by the anisotropic flow, as discussed in our previous publication [22]. The oscillations of R_{os}^2 decrease with k_T and R_l displays a negligible azimuthal angle dependence, which qualitatively agree with hydrodynamic calculations [35,45].

The data shown in Figs. 8 and 9 are fitted with the functions below to extract the oscillation strength [46],

$$R_\mu^2(\Delta\phi) = R_{\mu,0}^2 + 2R_{\mu,2}^2\cos(2\Delta\phi) \quad (\mu = s,o,l),$$
$$R_\mu^2(\Delta\phi) = 2R_{\mu,2}^2\sin(2\Delta\phi) \quad (\mu = os), \tag{13}$$

where $R_{\mu,2}^2$ are the second-order Fourier coefficient and $\Delta\phi = \phi - \Psi_2$. Detailed discussion on the oscillation amplitudes is presented in Sec. IV B 3.

2. *Blast-wave model fit*

In this section, we perform blast-wave (BW) model fits to our results to extract features at the kinetic freeze-out and study their particle species dependence. The BW model [47] is based on a hydrodynamical model parametrized by the freeze-out conditions, such as the freeze-out temperature

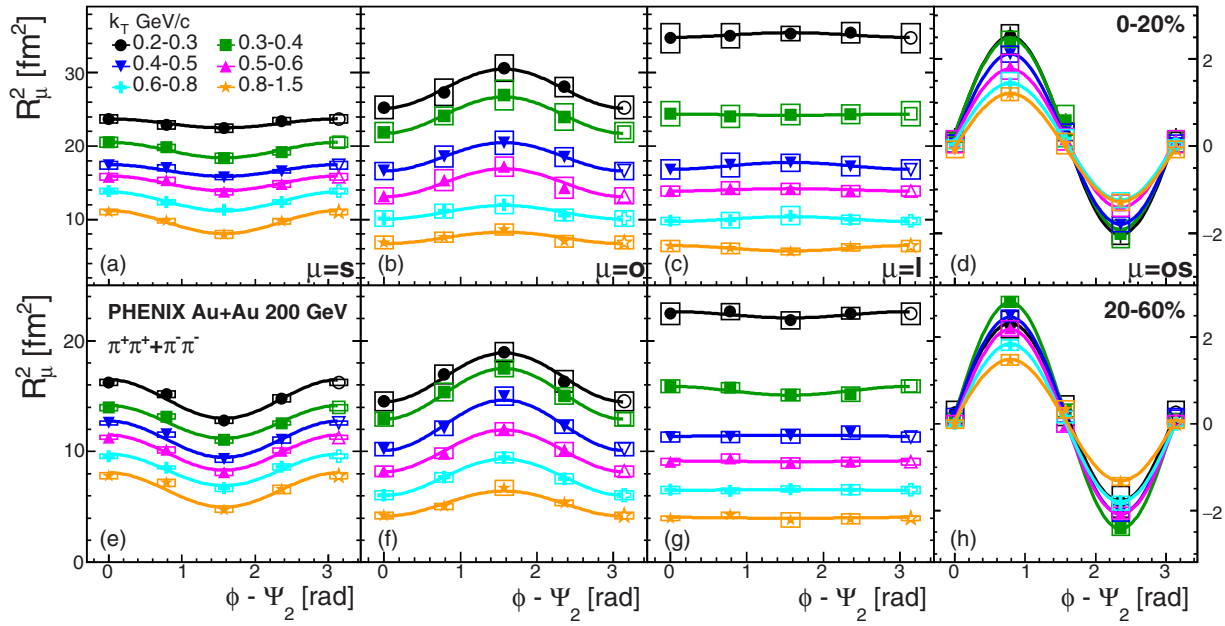

FIG. 9. (Color online) Squared HBT radii of charged-pion pairs as a function of azimuthal pair angle ϕ with respect to Ψ_2 for six k_T bins and two centrality bins [(a)–(d) for 0%–20% and (e)–(h) for 20%–60%], where open symbols at $\phi - \Psi_2 = \pi$ are the same data as those at $\phi - \Psi_2 = 0$. Open boxes show systematic uncertainties and solid lines show the fit functions by Eq. (13).

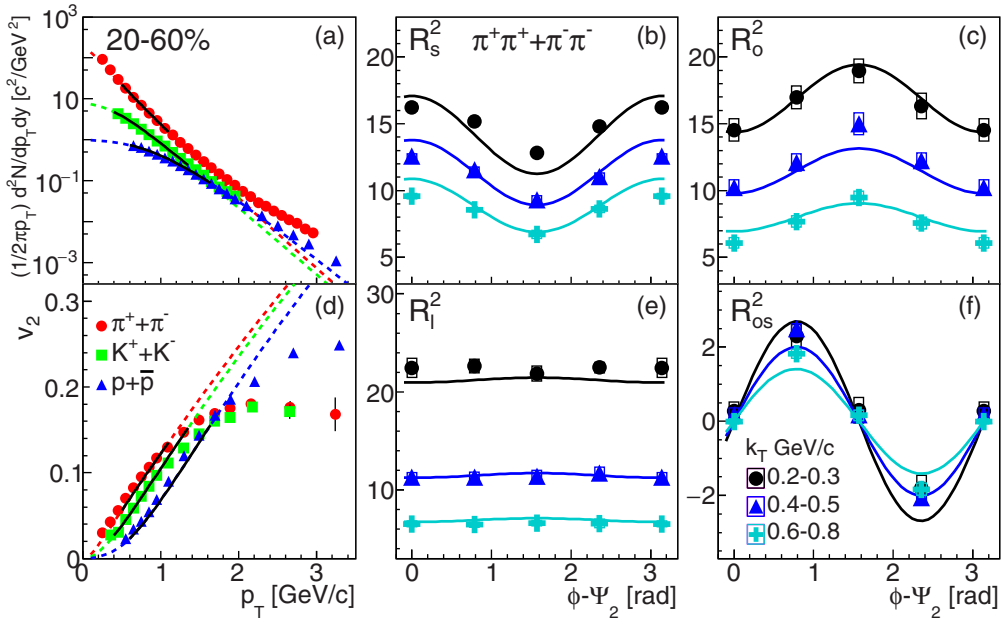

FIG. 10. (Color online) The BW model fits (Fit A) to the p_T spectra (a), elliptic flow of π, K, p (d), and HBT radii of π (b),(c),(e),(f). The solid lines show the fit functions.

(T_f) and the transverse flow rapidity (ρ_0). This model is further expanded in Ref. [35] to describe the elliptic flow and azimuthal angle dependence of HBT radii by introducing additional parameters: second-order modulation in transverse flow rapidity (ρ_2), the transverse source size (R_x, R_y), the freeze-out time (τ_0), and the emission duration ($\Delta\tau$). Once the above seven parameters are fixed, the p_T spectra, elliptic flow, and HBT radii can be calculated within the model.

Each freeze-out parameter has a different sensitivity to each experimental observable [35]. For example, the ρ_2 and the ratio of R_x and R_y are less sensitive to p_T spectra, but more sensitive to the elliptic flow and the azimuthal angle dependence of HBT radii. To effectively constrain those parameters, a fit to p_T spectra was first performed to determine T_f and ρ_0, then the other parameters were determined by simultaneous fit to the elliptic flow and azimuthal-dependent HBT radii. For the source size parameters, the R_x and R_y/R_x are actually used as the fitting parameters.

The BW model assumes that the freeze-out for all hadron species takes place at the same time, but the actual situation may be more complicated. To investigate how the extracted freeze-out parameters vary by particle species of HBT radii, the following fits were tested:

(A) fit for p_T spectra and v_2 of π, K, p along with HBT radii of π;
(B) fit for p_T spectra and v_2 of π, K, p along with HBT radii of K.

In the case of Fit B, both azimuthal-dependent and azimuthal-integrated HBT radii of charged kaons were included in the fit.

Figure 10 shows the results of Fit A for the p_T spectra [Fig. 10(a)] and elliptic flow [Fig. 10(d)] of π, K, and p, and pion HBT radii [Figs. 10(b), 10(c), 10(e), 10(f)] in 20%–60% centrality. The solid lines show the BW fitting functions and

TABLE III. Summary of extracted parameters in the BW model fit for two fitting conditions (see the text for details). The T_f and ρ_0 parameters were obtained by fits to p_T spectra, and the other parameters were obtained by a simultaneous fit to v_2 and the HBT radii. The values in parentheses represent the systematic uncertainties derived by varying the model fit conditions.

Fit	Centrality	T_f (MeV)	ρ_0	ρ_2	R_x (fm)	R_y/R_x	τ (fm/c)	$\Delta\tau$ (fm/c)	χ^2/NDF (spectra)	χ^2/NDF (v_2)	χ^2/NDF (HBT)
A	0%–20%	104	0.995	0.047	11.28	1.092	8.22	2.06	$143.4/27 = 5.3$	$25.2/21 = 1.2$	$2526.7/96 = 26.3$
		(5)	(0.055)	(0.005)	(0.23)	(0.003)	(0.23)	(0.18)			
A	20%–60%	113	0.905	0.074	8.25	1.171	6.1	1.56	$206.5/27 = 7.6$	$46.4/21 = 2.2$	$1998.3/96 = 20.8$
		(8)	(0.059)	(0.012)	(0.29)	(0.003)	(0.31)	(0.12)			
B	0%–20%	104	0.995	0.042	10.19	1.102	8.48	2.73	$143.4/27 = 5.3$	$11.0/21 = 0.5$	$116.9/28 = 4.2$
		(5)	(0.055)	(0.004)	(0.46)	(0.004)	(0.81)	(0.58)			
B	20%–60%	113	0.905	0.067	7.44	1.182	4.95	2.86	$206.5/27 = 7.6$	$39.4/21 = 1.9$	$95.7/28 = 3.4$
		(8)	(0.059)	(0.01)	(0.55)	(0.008)	(0.91)	(0.52)			

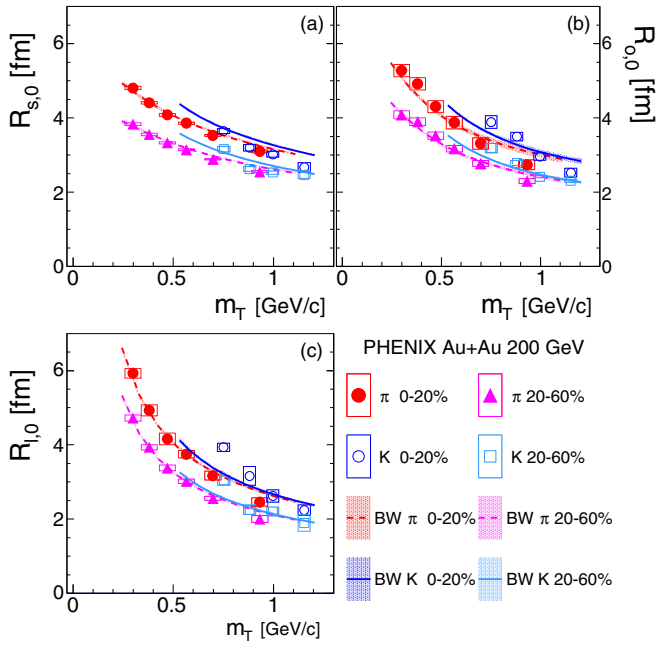

FIG. 11. (Color online) The zeroth-order Fourier coefficient of HBT radii of charged pions as a function of m_T and BW model calculations for both pions (dashed line) and kaons (solid line), where the BW model parameters shown in Fit A of Table III were used.

the dashed lines in panels (a) and (d) represent the extended fitting function beyond their actual fit ranges. Only three k_T bins for HBT radii are shown here, but all six k_T bins shown in Fig. 9 were simultaneously used in the fit. Here the data of p_T spectra are taken from Ref. [48] and the data of v_2 from Ref. [49]. The p_T spectra and v_2 are well described at low p_T, and the overall trend of the HBT radii is also reproduced by the BW model.

The results from the fits are summarized in Table III. The systematic uncertainties of the BW model fit were estimated by varying the fit conditions: the fit range, a surface diffuseness to control the density profile [35], and the relative weighting factor between different particle species. The systematic uncertainties of data were taken into account in the calculation of χ^2. Our results from Fit A are in good agreement with those in previous studies [37,50]. The results of Fit B shows slightly different values, i.e., smaller R_x and larger $\Delta\tau$. The smaller source (R_x) might be intuitively understood as owing to kaons freezing out earlier than pions, but it is not significant in the parameter τ. The $\Delta\tau$ obtained by the Fit B using the kaon HBT result shows relatively larger values than the results by Fit A, which is consistent with the result from R_o/R_s as shown in Fig. 4.

Also, the m_T dependence of the pion and kaon HBT radii has been calculated using the parameters obtained from Fit A, as shown with lines in Fig. 11. For a comparison, the zeroth-order Fourier coefficients ($R_{\mu,0}$) for pions which correspond to the HBT radii obtained in the azimuthal-integrated analysis are plotted as solid symbols. The kaon HBT radii from the azimuthal-integrated analysis are also compared in the figure. The BW model shows the π/K difference in the sidewards and outward directions, but not in the longitudinal direction, unlike the experimental data.

3. *Oscillation amplitudes with hydrodynamic models*

The BW model [35] suggests that the source eccentricity at freeze-out is given by $\varepsilon_{\rm final} = 2R^2_{s,2}/R^2_{s,0} = -2R^2_{o,2}/R^2_{s,0} = 2R^2_{os,2}/R^2_{s,0}$ [see Eq. (13)] in the absence of position-momentum correlation, i.e., radial flow. In the presence of radial flow, the above relation would be smeared because the HBT radius does not reflect the whole source size, but the $\varepsilon_{\rm final}$ from $R^2_{s,2}$ could still be a good estimator in the limit of $k_T = 0$.

The HBT radii of both pions and kaon averaged over the azimuthal direction are well described by the hydrodynamic models including the BW model, as shown so far. In this section, the oscillation amplitudes are also compared with the hydrodynamic models. The oscillation amplitudes were extracted by using Eq. (13). The systematic uncertainties were estimated by performing the fitting with Eq. (13) for the data of various systematic sources described in Sec. III E. In Figs. 12 and 13, the oscillation amplitudes with four different combinations of HBT radii are plotted in the form of a final eccentricity, $2R^2_{\mu,2}/R^2_{\nu,0}$, where μ and ν denote o,s,os. The $R^2_{\mu,2}$ is a fitting parameter in Eq. (13) that can take a negative

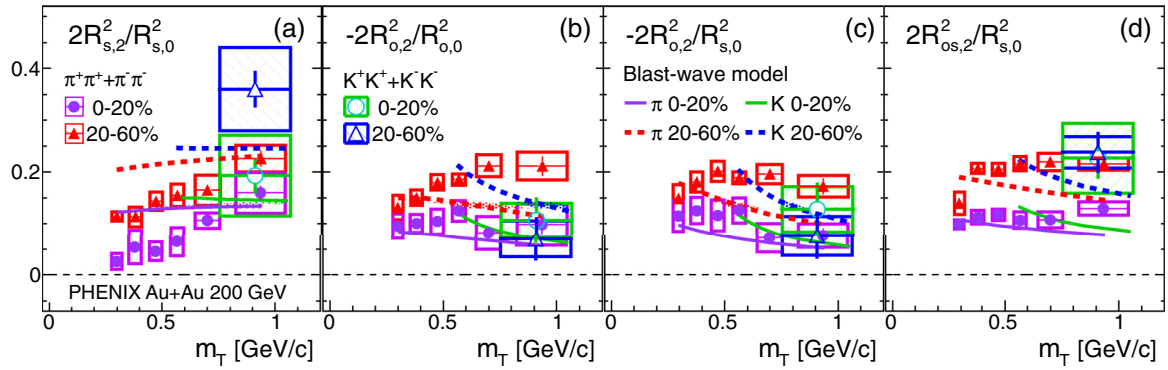

FIG. 12. (Color online) Oscillation amplitudes relative to the average for four different combinations of the azimuthal-dependent HBT radii as a function of m_T for charged pions and kaons. Open boxes show systematic uncertainties. Calculations from the BW model with parameters of Fit A shown in Table III are shown for comparison.

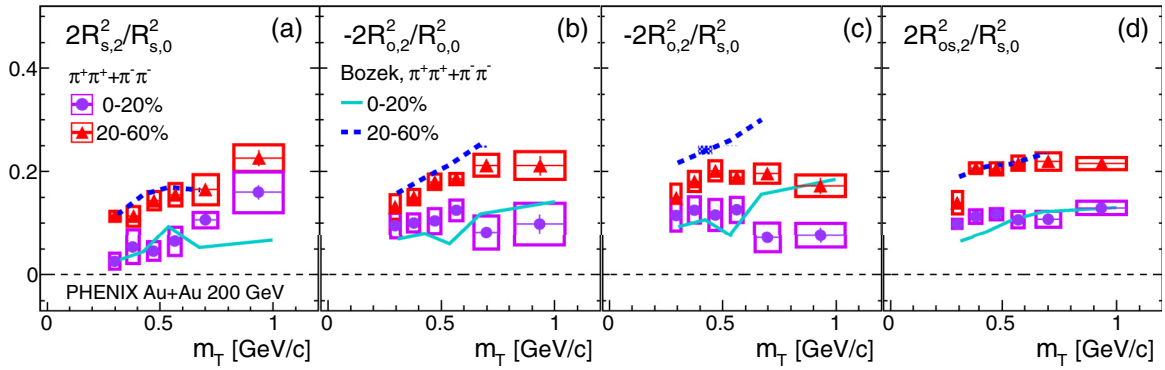

FIG. 13. (Color online) Oscillation amplitudes relative to the average for four different combinations of the azimuthal-dependent HBT radii as a function of m_T for charged pions. Open boxes show systematic uncertainties. Calculations from the 3 + 1-D viscous-hydrodynamic model [39] are shown for comparison.

value, which represents a different phase of the cosine function and shown in Figs. 12(b), 12(c), 13(b), and 13(c).

Figure 12(a) shows the oscillation amplitude of R^2_s relative to the average, which is most sensitive to the final source eccentricity. The value of $2R^2_{s,2}/R^2_{s,0}$ increases with m_T, which would reflect m_T-dependent ellipticity of the emission region. The other combinations of $|2R^2_{\mu,2}/R^2_{\nu,2}|$ show similar m_T dependence, but less dependence especially in 0%–20% centrality. It should be noted that the R_o and R_{os} contain the particle emission duration in addition to the geometrical information, and they are also dominated by the anisotropy in the expansion velocity.

The data are compared with the BW calculation using the Fit A parameters in Fig. 12. The dependency on m_T of the oscillation amplitudes is not described well, although the m_T dependence of the mean radii is reproduced well. The large χ^2 of HBT in Fit A in Table III is mainly caused by such a discrepancy. The calculations from the event-by-event 3 + 1-D viscous-hydrodynamic model [39] with a Glauber initial condition and shear viscosity $\eta/s = 0.08$ (and also nonzero bulk viscosity) are compared to the same data in Fig. 13. The model employs the equation of state with a crossover transition, but does not include a hadron cascade. The model quantitatively agrees with the data of R_s and R_{os} but overestimates R_o in 20%–60%, although the trend (not the magnitude) of dependency on m_T is reproduced in contrast with the BW model.

When data points of kaons are compared to those of pions in the 0%–20% centrality sample, they mostly agree within the systematic uncertainties, but in the 20%–60% sample the $2R^2_{s,2}/R^2_{s,0}$ ($2R^2_{o,2}/R^2_{o,0}$) of kaons is slightly larger (smaller) than that of pions. More precise measurement is needed to confirm the difference.

V. SUMMARY AND CONCLUSION

We have presented results from the PHENIX experiment on charged-pion and kaon femtoscopy measurements in Au + Au collisions at $\sqrt{s_{NN}} = 200$ GeV. In the azimuthal-integrated analysis, we have measured the HBT radii of both species with fine m_T and centrality bins. m_T scaling holds well for R_s, but there are visible differences for R_o and R_l between charged pions and kaons at the same m_T, and the differences become larger in more central collisions. m_T scaling breaks for those radii, but k_T scaling works well for all radii. It is observed that the ratio R_o/R_s of kaons is larger than that of pions, which may imply different emission durations. The HKM was compared with our data. It reproduces most aspects of the data of both charged pions and kaons, but it fails to accurately describe the difference in R_o.

In the azimuthal-dependent analysis, a first measurement of the HBT radii of charged kaons with respect to the second-order event plane has been performed and compared with pion measurements with finer m_T bins. Oscillation with respect to the event plane of kaon HBT radii has been clearly observed and is similar to that of pions. The data were compared with the BW model and the 3 + 1-D viscous-hydrodynamic model. The BW model provides a good description of the overall trend of the p_T spectra, the elliptic flow, and the mean HBT radii, but fails to describe the details of femtoscopy measurements, such as the m_T-dependent oscillation amplitude of the source radii. While the 3 + 1-D viscous-hydrodynamic model does qualitatively reproduce the data, it overestimates the oscillation of R_o. We note that the viscous hydrodynamic model also reproduces well the other observables such as the p_T spectra and elliptic flow [51].

Both the HKM and the viscous-hydrodynamic model surprisingly describe all aspects of the femtoscopic data, even though these models lack the shear viscosity of plasma and the microscopic transport phase. Including these effects may improve the description of the measured R_o/R_s and $R^2_{o,2}$. More precise measurements and systematic model comparison for both azimuthal-dependent and azimuthal-integrated HBT measurements are needed. The particle-species dependence, in addition to the differential femtoscopy measurements may, help to elucidate the expansion dynamics of heavy-ion collisions.

ACKNOWLEDGMENTS

We thank the staff of the Collider-Accelerator and Physics Departments at Brookhaven National Laboratory and the staff of the other PHENIX participating institutions for their vital contributions. We acknowledge support from the Office of

Nuclear Physics in the Office of Science of the Department of Energy, the National Science Foundation, Abilene Christian University Research Council, Research Foundation of SUNY, and the Dean of the College of Arts and Sciences, Vanderbilt University (USA); Ministry of Education, Culture, Sports, Science, and Technology and the Japan Society for the Promotion of Science (Japan); Conselho Nacional de Desenvolvimento Científico e Tecnológico and Fundação de Amparo à Pesquisa do Estado de São Paulo (Brazil); Natural Science Foundation of China (People's Republic of China); Ministry of Science, Education, and Sports (Croatia); Ministry of Education, Youth and Sports (Czech Republic); Centre National de la Recherche Scientifique, Commissariat à l'Énergie Atomique, and Institut National de Physique Nucléaire et de Physique des Particules (France); Bundesministerium für Bildung und Forschung, Deutscher Akademischer Austausch Dienst, and Alexander von Humboldt Stiftung (Germany); National Science Fund, OTKA, Károly Róbert University College, and the Charles Simonyi Fund (Hungary); Department of Atomic Energy and Department of Science and Technology (India); Israel Science Foundation (Israel); Basic Science Research Program through NRF of the Ministry of Education (Korea); Physics Department, Lahore University of Management Sciences (Pakistan); Ministry of Education and Science, Russian Academy of Sciences, Federal Agency of Atomic Energy (Russia); VR and Wallenberg Foundation (Sweden); the US Civilian Research and Development Foundation for the Independent States of the Former Soviet Union; the Hungarian American Enterprise Scholarship Fund; and the United States-Israel Binational Science Foundation.

APPENDIX A: BLAST-WAVE MODEL

An emission function in the BW parametrization for bosons [35] is given by

$$S(r,\phi_s,\tau,\eta) = m_T \cosh(\eta - y)\Omega(r,\phi_s)e^{-(\tau-\tau_0)^2/(2\Delta\tau^2)} \times \sum_{n=1}^{\infty} e^{n\alpha\cos(\phi_b-\phi_p)}e^{-n\beta\cosh(\eta-y)}, \quad \text{(A1)}$$

where m_T is the transverse mass, y is rapidity, ϕ_p is azimuthal angle of particle momentum, and α and β are defined as

$$\alpha = \frac{p_T}{T}\sinh\rho(r,\phi_s), \quad \text{(A2)}$$

$$\beta = \frac{m_T}{T}\cosh\rho(r,\phi_s). \quad \text{(A3)}$$

The transverse rapidity $\rho(r,\phi_s)$ is defined as

$$\rho(r,\phi_s) = [\rho_0 + \rho_2\cos(2\phi_b)]\tilde{r}, \qquad \tilde{r} = \sqrt{(x/R_x)^2 + (y/R_y)^2}, \quad \text{(A4)}$$

where x and y are space coordinates of particles, ϕ_s is azimuthal angle of the spatial positions, and ϕ_b is a boost direction. It is assumed that particles are boosted to the direction perpendicular to the elliptical subshell of the particle-emitting source, which satisfies the relation

$$\tan(\phi_s) = (R_y/R_x)^2\tan(\phi_b). \quad \text{(A5)}$$

The distribution of the source elements $\Omega(\tilde{r})$ is given by

$$\Omega(\tilde{r}) = 1/(1 + e^{(\tilde{r}-1)/a}), \quad \text{(A6)}$$

where a denotes a surface diffuseness and $a = 0$ gives a box profile and $a = 0.3$ gives approximately a Gaussian profile. Observables, such as spectra, v_2, and HBT radii, are obtained by performing the integral of the emission function Eq. (A1) over phase space weighted with certain quantity B:

$$\int d^4x, S(x,K)B(x,K) = \int_0^{2\pi} d\phi_s \int_0^{\infty} r dr \int_{-\infty}^{\infty} d\eta \int_{-\infty}^{\infty} \times \tau d\tau S(r,\phi_s,\tau,\eta)B(x,K). \quad \text{(A7)}$$

Azimuthally integrated p_T spectra can be obtained by integrating over ϕ_p and τ in Eq. (A8) setting $B(x,K)$=1. If we assume Boltzmann distribution for all particles, only the first term in the summation in Eq. (A1) is used. Also, in case of analyzing particles in midrapidity region, Eq. (A1) can be simplified by setting $y = 0$. Then Eq. (A8) can be rewritten as

$$\begin{aligned}\frac{dN}{p_T dp_T} &= \sqrt{2\pi}\tau_0\Delta\tau \int_0^{2\pi} d\phi_p \int_0^{2\pi} d\phi_s \int_0^{\infty} r dr \int_{-\infty}^{\infty} d\eta \\ &\quad \times m_T \cosh(\eta)\Omega(r,\phi_s)e^{\alpha\cos(\phi_b-\phi_p)}e^{-\beta\cosh(\eta)} \\ &= 2\sqrt{2\pi}\,\tau_0\Delta\tau \int_0^{2\pi} d\phi_p \int_0^{2\pi} d\phi_s \int_0^{\infty} r dr \\ &\quad \times m_T\Omega(r,\phi_s)\, e^{\alpha\cos(\phi_b-\phi_p)}K_1(\beta), \end{aligned} \quad \text{(A8)}$$

where $K_n(\beta)$ is the modified Bessel function of the second kind, which is defined as

$$K_n(z) = \frac{1}{2}\int_{-\infty}^{\infty} dt\cosh(nt)e^{-z\cosh(t)}. \quad \text{(A9)}$$

Here we replace $\phi_b - \phi_p$ as ϕ', and the range of the integral over ϕ' is from ϕ_b to $\phi_b - 2\pi$. Then the range can be replaced from 0 to 2π because the integrand is the periodic function with 2π. Finally, Eq. (A8) is rewritten as

$$\frac{dN}{p_T dp_T} = 2(2\pi)^{3/2}\tau_0\Delta\tau m_T \times \int_0^{2\pi} d\phi_s \int_0^{\infty} r dr\,\Omega(r,\phi_s)\, I_0(\alpha)K_1(\beta), \quad \text{(A10)}$$

where I_n is the modified Bessel function of the first kind given by

$$I_n(z) = \frac{1}{2\pi}\int_0^{2\pi} dt\cos(nt)e^{-z\cos(t)}. \quad \text{(A11)}$$

The elliptic flow v_2 is calculated as

$$v_2(p_T,m) = \frac{\int d\phi_p \int d^4x\cos(2\phi_p)S(x,K)}{\int d\phi_p \int d^4x\, S(x,K)}. \quad \text{(A12)}$$

The denominator is the same expression with Eq. (A10). The numerator can be calculated by a similar way to derive

the p_T spectra,

$$\begin{aligned}
&\int d\phi_p \int d^4x \cos(2\phi_p) S(x,K) \\
&= 2\sqrt{2\pi}\,\tau_0 \Delta\tau \int_0^{2\pi} d\phi_p \int_0^{2\pi} d\phi_s \\
&\quad \times \int_0^{\infty} r dr m_T \Omega(r,\phi_s) \cos(2\phi_p) e^{\alpha \cos(\phi_b - \phi_p)} K_1(\beta) \\
&= 2\sqrt{2\pi}\,\tau_0 \Delta\tau \int_0^{2\pi} d\phi_p \\
&\quad \times \int_0^{\infty} r dr m_T\, \Omega(r,\phi_s) K_1(\beta) \cos(2\phi_b) \\
&\quad \times \int_0^{2\pi} d\phi' \cos(2\phi') e^{\alpha \cos(\phi')} \\
&= 2(2\pi)^{3/2}\,\tau_0 \Delta\tau m_T \int_0^{2\pi} d\phi_p \\
&\quad \times \int_0^{\infty} r dr \Omega(r,\phi_s) K_1(\beta) \cos(2\phi_b) I_2(\alpha). \qquad \text{(A13)}
\end{aligned}$$

Finally, the elliptic flow can be expressed as

$$v_2(p_T,m) = \frac{\int_0^{2\pi} d\phi_p \int_0^{\infty} r dr \Omega(r,\phi_s) K_1(\beta) \cos(2\phi_b) I_2(\alpha)}{\int_0^{2\pi} d\phi_s \int_0^{\infty} r dr \Omega(r,\phi_s)\, I_0(\alpha) K_1(\beta)}. \qquad \text{(A14)}$$

The HBT radii are related to space-time variance as [35]

$$\begin{aligned}
R_{\rm s}^2 &= \tfrac{1}{2}(\langle\tilde{x}^2\rangle + \langle\tilde{y}^2\rangle) - \tfrac{1}{2}(\langle\tilde{x}^2\rangle - \langle\tilde{y}^2\rangle)\cos(2\phi_p) \\
&\quad - \langle\tilde{x}\tilde{y}\rangle \sin(2\phi_p), \qquad \text{(A15)} \\
R_{\rm o}^2 &= \tfrac{1}{2}(\langle\tilde{x}^2\rangle + \langle\tilde{y}^2\rangle) + \tfrac{1}{2}(\langle\tilde{x}^2\rangle - \langle\tilde{y}^2\rangle)\cos(2\phi_p) \\
&\quad + \langle\tilde{x}\tilde{y}\rangle \sin(2\phi_p) - 2\beta_T(\langle\tilde{t}\tilde{x}\rangle \cos\phi_p + \langle\tilde{t}\tilde{y}\rangle \sin\phi_p) \\
&\quad + \beta_T^2\langle\tilde{t}^2\rangle, \qquad \text{(A16)} \\
R_{\rm os}^2 &= \langle\tilde{x}\tilde{y}\rangle \cos(2\phi_p) - \tfrac{1}{2}(\langle\tilde{x}^2\rangle - \langle\tilde{y}^2\rangle)\sin(2\phi_p) \\
&\quad + \beta_T(\langle\tilde{t}\tilde{x}\rangle \sin\phi_p - \langle\tilde{t}\tilde{y}\rangle \cos\phi_p), \qquad \text{(A17)} \\
R_{\rm l}^2 &= \langle\tilde{z}^2\rangle - 2\beta_l\langle\tilde{t}\tilde{z}\rangle + \beta_l^2\langle\tilde{t}^2\rangle = \langle\tilde{z}^2\rangle, \qquad \text{(A18)}
\end{aligned}$$

where

$$\langle f(x)\rangle = \frac{\int d^4x f(x) S(x,K)}{\int d^4x S(x,K)}, \qquad \text{(A19)}$$

$$\tilde{x}^\mu = x^\mu - \langle x^\mu\rangle, \qquad \text{(A20)}$$

and β_l vanishes in the longitudinally comoving system frame and the terms including t and z depend on the proper time τ and emission duration of particles $\Delta\tau$. As shown in above equations, $R_{\rm s}$ depends on only the spatial extent of the source and azimuthal angle ϕ_p, while $R_{\rm o}$ and $R_{\rm os}$ are also sensitive to τ and $\Delta\tau$, as well as the spatial extent.

APPENDIX B: DATA TABLES

The extracted HBT radii and the oscillation amplitudes for charged pion and kaons in Au + Au collisions at $\sqrt{s_{NN}} =$ 200 GeV are summarized in Tables IV–XI.

TABLE IV. HBT parameters of positive pion pairs, shown as value ± statistical uncertainty (absolute value) ± systematic uncertainty (%), for the centrality bins shown in Fig. 3.

Centrality	$\langle m_T\rangle$ (GeV/c)	λ	$R_{\rm s}$ (fm)	$R_{\rm o}$ (fm)	$R_{\rm l}$ (fm)
0%–10%	0.3	0.292 ± 0.003 ± 11.1	5.11 ± 0.03 ± 0.5	5.55 ± 0.04 ± 2.9	6.3 ± 0.04 ± 2.3
	0.36	0.358 ± 0.004 ± 8.7	4.76 ± 0.03 ± 0.6	5.22 ± 0.03 ± 3	5.41 ± 0.04 ± 2.8
	0.41	0.392 ± 0.004 ± 6.1	4.52 ± 0.03 ± 0.8	4.91 ± 0.03 ± 2.8	4.8 ± 0.04 ± 3.7
	0.47	0.402 ± 0.005 ± 11	4.28 ± 0.03 ± 1.3	4.51 ± 0.03 ± 4.7	4.31 ± 0.03 ± 5.2
	0.53	0.45 ± 0.006 ± 7.3	4.17 ± 0.03 ± 0.7	4.21 ± 0.04 ± 4.2	4.08 ± 0.04 ± 4.2
	0.59	0.454 ± 0.007 ± 5.9	3.98 ± 0.03 ± 1.4	3.97 ± 0.04 ± 5.7	3.8 ± 0.04 ± 3.2
	0.66	0.458 ± 0.007 ± 4.7	3.77 ± 0.03 ± 1.1	3.62 ± 0.04 ± 4.8	3.45 ± 0.04 ± 4.8
	0.79	0.462 ± 0.008 ± 6.1	3.47 ± 0.03 ± 1.2	3.27 ± 0.04 ± 4.9	3.01 ± 0.04 ± 5.2
	0.96	0.447 ± 0.016 ± 12	3.16 ± 0.06 ± 3.1	2.91 ± 0.07 ± 10.9	2.49 ± 0.06 ± 6.1
	1.16	0.448 ± 0.034 ± 18.5	2.93 ± 0.11 ± 8.3	2.4 ± 0.12 ± 14.4	2.13 ± 0.11 ± 9.4
10%–20%	0.3	0.313 ± 0.003 ± 9	4.63 ± 0.03 ± 0.6	5.01 ± 0.03 ± 2.4	5.77 ± 0.04 ± 1.9
	0.36	0.379 ± 0.004 ± 7.2	4.3 ± 0.03 ± 0.5	4.74 ± 0.03 ± 2.6	4.95 ± 0.04 ± 2.8
	0.41	0.41 ± 0.004 ± 7.3	4.1 ± 0.03 ± 1.3	4.41 ± 0.03 ± 3.1	4.44 ± 0.03 ± 3.5
	0.47	0.441 ± 0.005 ± 7.5	3.94 ± 0.03 ± 1	4.12 ± 0.03 ± 3.6	4.07 ± 0.03 ± 4.2
	0.53	0.487 ± 0.006 ± 6.6	3.83 ± 0.03 ± 0.8	3.88 ± 0.03 ± 2.9	3.83 ± 0.03 ± 3.7
	0.59	0.501 ± 0.008 ± 5.5	3.67 ± 0.03 ± 0.9	3.68 ± 0.04 ± 3.7	3.56 ± 0.04 ± 2.3
	0.66	0.501 ± 0.008 ± 4.2	3.5 ± 0.03 ± 1.5	3.38 ± 0.03 ± 3.7	3.24 ± 0.03 ± 3.5
	0.79	0.501 ± 0.008 ± 4.3	3.21 ± 0.03 ± 0.9	2.99 ± 0.03 ± 4.9	2.78 ± 0.03 ± 3.1
	0.96	0.515 ± 0.016 ± 8.2	2.94 ± 0.05 ± 1.4	2.78 ± 0.06 ± 4.1	2.34 ± 0.05 ± 6.3
	1.16	0.52 ± 0.035 ± 11.2	2.76 ± 0.1 ± 9	2.23 ± 0.1 ± 2.8	2.09 ± 0.1 ± 9.7

TABLE IV. (*Continued.*)

Centrality	$\langle m_T \rangle$ (GeV/c)	λ	R_s (fm)	R_o (fm)	R_l (fm)
20%–40%	0.3	0.339 ± 0.003 ± 7.2	4.09 ± 0.02 ± 0.6	4.34 ± 0.02 ± 2.5	5.01 ± 0.03 ± 1.5
	0.36	0.401 ± 0.003 ± 5.8	3.81 ± 0.02 ± 0.9	4.09 ± 0.02 ± 2	4.35 ± 0.03 ± 2.1
	0.41	0.433 ± 0.004 ± 5.4	3.63 ± 0.02 ± 0.7	3.87 ± 0.02 ± 2.3	3.88 ± 0.03 ± 2.2
	0.47	0.46 ± 0.005 ± 6.9	3.5 ± 0.02 ± 0.9	3.59 ± 0.02 ± 3.2	3.55 ± 0.03 ± 3.7
	0.53	0.493 ± 0.005 ± 5.8	3.39 ± 0.02 ± 0.8	3.38 ± 0.02 ± 2.9	3.3 ± 0.03 ± 3
	0.59	0.519 ± 0.007 ± 3.7	3.26 ± 0.02 ± 0.3	3.2 ± 0.03 ± 2.7	3.11 ± 0.03 ± 2.1
	0.66	0.505 ± 0.006 ± 3.2	3.07 ± 0.02 ± 0.4	2.91 ± 0.02 ± 2.7	2.77 ± 0.03 ± 1.9
	0.79	0.532 ± 0.007 ± 3.5	2.89 ± 0.02 ± 1.1	2.66 ± 0.02 ± 3.7	2.45 ± 0.02 ± 3.1
	0.96	0.54 ± 0.014 ± 7.7	2.63 ± 0.04 ± 4.3	2.34 ± 0.04 ± 3.5	2.07 ± 0.04 ± 3.2
	1.16	0.554 ± 0.027 ± 4.3	2.35 ± 0.08 ± 2.9	2.09 ± 0.08 ± 5.5	1.76 ± 0.07 ± 5.6
40%–70%	0.3	0.363 ± 0.004 ± 5.8	3.27 ± 0.02 ± 0.9	3.39 ± 0.03 ± 2.6	3.94 ± 0.03 ± 1.1
	0.36	0.426 ± 0.005 ± 2.8	3.05 ± 0.03 ± 0.6	3.29 ± 0.03 ± 1.7	3.42 ± 0.03 ± 1.1
	0.41	0.455 ± 0.006 ± 4.2	2.92 ± 0.03 ± 0.7	3.16 ± 0.03 ± 3	3.09 ± 0.03 ± 1.5
	0.47	0.493 ± 0.007 ± 3.6	2.87 ± 0.03 ± 1.2	2.94 ± 0.03 ± 1.7	2.89 ± 0.03 ± 2.1
	0.53	0.509 ± 0.008 ± 3.9	2.73 ± 0.03 ± 0.9	2.81 ± 0.03 ± 1.8	2.63 ± 0.03 ± 2
	0.59	0.54 ± 0.01 ± 3.4	2.7 ± 0.03 ± 1.2	2.67 ± 0.04 ± 1.7	2.46 ± 0.04 ± 1.6
	0.66	0.569 ± 0.01 ± 1.2	2.61 ± 0.03 ± 2.1	2.48 ± 0.03 ± 1.9	2.31 ± 0.03 ± 1
	0.79	0.551 ± 0.01 ± 4.6	2.36 ± 0.03 ± 1.6	2.1 ± 0.03 ± 2.1	1.93 ± 0.03 ± 2.1
	0.96	0.619 ± 0.024 ± 5.7	2.35 ± 0.06 ± 1	1.99 ± 0.06 ± 4.4	1.82 ± 0.06 ± 1.6
	1.16	0.592 ± 0.041 ± 3.8	2.02 ± 0.13 ± 2.8	1.64 ± 0.13 ± 11.1	1.45 ± 0.11 ± 3.5

TABLE V. HBT parameters of negative pion pairs, shown as value ± statistical uncertainty (absolute value) ± systematic uncertainty (%), for the centrality bins shown in Fig. 3.

Centrality	$\langle m_T \rangle$ (GeV/c)	λ	R_s (fm)	R_o (fm)	R_l (fm)
0%–10%	0.3	0.275 ± 0.003 ± 10.5	5.11 ± 0.03 ± 0.6	5.49 ± 0.04 ± 3	6.28 ± 0.05 ± 2.9
	0.36	0.353 ± 0.004 ± 7.3	4.74 ± 0.03 ± 0.7	5.25 ± 0.04 ± 2.1	5.44 ± 0.05 ± 3.4
	0.41	0.387 ± 0.005 ± 7.9	4.5 ± 0.03 ± 0.4	4.91 ± 0.04 ± 3.6	4.82 ± 0.04 ± 3.9
	0.47	0.399 ± 0.005 ± 9.1	4.31 ± 0.03 ± 0.9	4.38 ± 0.04 ± 4.3	4.29 ± 0.04 ± 5.4
	0.53	0.444 ± 0.007 ± 4.7	4.17 ± 0.03 ± 1.2	4.19 ± 0.04 ± 3.6	4.11 ± 0.04 ± 3
	0.59	0.45 ± 0.008 ± 7.4	3.95 ± 0.04 ± 1.2	3.91 ± 0.04 ± 5.7	3.82 ± 0.04 ± 3.8
	0.66	0.451 ± 0.008 ± 7.3	3.77 ± 0.03 ± 0.2	3.61 ± 0.04 ± 5.3	3.47 ± 0.04 ± 3.3
	0.79	0.442 ± 0.008 ± 6.2	3.49 ± 0.03 ± 1	3.16 ± 0.04 ± 6	2.96 ± 0.04 ± 5.5
	0.96	0.437 ± 0.017 ± 5	3.22 ± 0.07 ± 2.4	2.78 ± 0.07 ± 4.5	2.46 ± 0.06 ± 6.9
	1.15	0.526 ± 0.046 ± 13.3	3.1 ± 0.13 ± 3.1	2.27 ± 0.13 ± 8.1	2.43 ± 0.13 ± 11.1
10%–20%	0.3	0.295 ± 0.003 ± 9.4	4.63 ± 0.03 ± 0.4	4.93 ± 0.04 ± 3.4	5.74 ± 0.04 ± 2.3
	0.36	0.363 ± 0.004 ± 6.4	4.3 ± 0.03 ± 0.3	4.71 ± 0.04 ± 3.1	4.88 ± 0.04 ± 2.6
	0.41	0.404 ± 0.005 ± 6.9	4.13 ± 0.03 ± 0.5	4.42 ± 0.04 ± 2.8	4.46 ± 0.04 ± 3.6
	0.47	0.443 ± 0.006 ± 7.2	3.95 ± 0.03 ± 1	4.13 ± 0.03 ± 2.9	4.05 ± 0.04 ± 4.1
	0.53	0.462 ± 0.007 ± 5.9	3.8 ± 0.03 ± 0.2	3.91 ± 0.04 ± 3.4	3.77 ± 0.04 ± 2.8
	0.59	0.492 ± 0.008 ± 4.1	3.68 ± 0.03 ± 0.4	3.64 ± 0.04 ± 3.7	3.53 ± 0.04 ± 3.5
	0.66	0.48 ± 0.008 ± 4.7	3.47 ± 0.03 ± 1.2	3.33 ± 0.03 ± 4.3	3.15 ± 0.03 ± 3.8
	0.79	0.497 ± 0.009 ± 5.1	3.25 ± 0.03 ± 0.5	3.01 ± 0.03 ± 4	2.75 ± 0.03 ± 3.7
	0.96	0.482 ± 0.016 ± 3.6	2.89 ± 0.05 ± 1.2	2.68 ± 0.06 ± 4.5	2.27 ± 0.05 ± 5.2
	1.15	0.579 ± 0.043 ± 16.5	2.67 ± 0.12 ± 8.6	2.29 ± 0.11 ± 5.7	2.11 ± 0.1 ± 6.7
20%–40%	0.3	0.32 ± 0.003 ± 6.8	4.11 ± 0.02 ± 0.5	4.28 ± 0.03 ± 2.3	5.05 ± 0.03 ± 2
	0.36	0.385 ± 0.004 ± 7.3	3.83 ± 0.03 ± 1.4	4.03 ± 0.03 ± 2.8	4.32 ± 0.03 ± 2.1
	0.41	0.429 ± 0.005 ± 5	3.65 ± 0.02 ± 0.5	3.89 ± 0.03 ± 1.3	3.93 ± 0.03 ± 2.5
	0.47	0.458 ± 0.005 ± 6.6	3.5 ± 0.02 ± 0.5	3.59 ± 0.03 ± 3.1	3.54 ± 0.03 ± 3.5
	0.53	0.487 ± 0.006 ± 4.5	3.4 ± 0.03 ± 0.7	3.38 ± 0.03 ± 1.8	3.32 ± 0.03 ± 2.7
	0.59	0.509 ± 0.007 ± 3.5	3.26 ± 0.03 ± 0.9	3.18 ± 0.03 ± 2.7	3.1 ± 0.03 ± 2.9
	0.66	0.521 ± 0.007 ± 2.5	3.11 ± 0.02 ± 0.6	2.96 ± 0.03 ± 2.6	2.86 ± 0.03 ± 2.2
	0.79	0.521 ± 0.007 ± 4.8	2.87 ± 0.02 ± 0.7	2.62 ± 0.03 ± 3	2.4 ± 0.02 ± 3
	0.96	0.536 ± 0.015 ± 2.2	2.66 ± 0.04 ± 1.1	2.31 ± 0.04 ± 3	2.05 ± 0.04 ± 3.3
	1.16	0.565 ± 0.034 ± 8.6	2.45 ± 0.1 ± 3.4	1.97 ± 0.09 ± 1.7	1.81 ± 0.09 ± 3.3

TABLE V. (*Continued.*)

Centrality	$\langle m_T \rangle$ (GeV/c)	λ	R_s (fm)	R_o (fm)	R_l (fm)
40%–70%	0.3	0.344 ± 0.004 ± 5.2	3.25 ± 0.03 ± 0.9	3.31 ± 0.03 ± 1.5	3.96 ± 0.04 ± 0.7
	0.36	0.409 ± 0.006 ± 4.3	3.05 ± 0.03 ± 0.9	3.27 ± 0.03 ± 1.9	3.41 ± 0.04 ± 1.8
	0.41	0.452 ± 0.007 ± 3.1	2.92 ± 0.03 ± 1	3.15 ± 0.03 ± 2.3	3.1 ± 0.04 ± 1.3
	0.47	0.489 ± 0.008 ± 4.8	2.83 ± 0.03 ± 1.4	2.95 ± 0.03 ± 2.6	2.86 ± 0.04 ± 1.8
	0.53	0.528 ± 0.009 ± 2.5	2.8 ± 0.03 ± 1.1	2.77 ± 0.03 ± 2	2.67 ± 0.04 ± 2.2
	0.59	0.539 ± 0.011 ± 2.9	2.65 ± 0.04 ± 2.3	2.62 ± 0.04 ± 3.2	2.47 ± 0.04 ± 1.3
	0.66	0.532 ± 0.01 ± 4.6	2.5 ± 0.03 ± 2	2.4 ± 0.03 ± 2.6	2.25 ± 0.03 ± 3.7
	0.79	0.565 ± 0.012 ± 3.5	2.41 ± 0.03 ± 1.4	2.19 ± 0.04 ± 1.7	1.99 ± 0.03 ± 2.5
	0.96	0.582 ± 0.023 ± 7.7	2.26 ± 0.07 ± 2.2	1.91 ± 0.07 ± 3.9	1.7 ± 0.06 ± 3.5
	1.15	0.641 ± 0.063 ± 3.5	2.18 ± 0.17 ± 9	1.72 ± 0.14 ± 10.9	1.67 ± 0.15 ± 17.3

TABLE VI. HBT parameters of charge-combined kaon pairs, shown as value ± statistical uncertainty (absolute value) ± systematic uncertainty (%), for the centrality bins shown in Fig. 3.

Centrality	$\langle m_T \rangle$ (GeV/c)	λ	R_s (fm)	R_o (fm)	R_l (fm)
0%–10%	0.76	0.507 ± 0.044 ± 12.9	3.8 ± 0.15 ± 2.7	4.07 ± 0.15 ± 5	4.09 ± 0.17 ± 2.9
	0.91	0.46 ± 0.043 ± 12.7	3.32 ± 0.13 ± 4.9	3.49 ± 0.15 ± 5.3	3.25 ± 0.17 ± 4.1
	1.1	0.404 ± 0.043 ± 4.3	2.86 ± 0.14 ± 3.4	3.1 ± 0.18 ± 5.4	2.36 ± 0.15 ± 7.7
10%–20%	0.76	0.539 ± 0.044 ± 11.3	3.37 ± 0.13 ± 2.6	3.56 ± 0.13 ± 4	3.55 ± 0.16 ± 4.5
	0.91	0.515 ± 0.044 ± 15.3	3.03 ± 0.12 ± 2.7	3.2 ± 0.13 ± 1.2	2.98 ± 0.14 ± 12.5
	1.1	0.457 ± 0.052 ± 14.7	2.75 ± 0.14 ± 1.5	2.48 ± 0.14 ± 2.6	2.34 ± 0.17 ± 10.8
20%–40%	0.76	0.64 ± 0.044 ± 11.4	3.18 ± 0.11 ± 2	3.28 ± 0.1 ± 4	3.15 ± 0.12 ± 4.7
	0.91	0.489 ± 0.034 ± 7.6	2.69 ± 0.1 ± 2.8	2.73 ± 0.1 ± 3	2.29 ± 0.11 ± 3.8
	1.09	0.501 ± 0.046 ± 13.9	2.56 ± 0.13 ± 3.8	2.31 ± 0.12 ± 3.2	2.05 ± 0.13 ± 7.4
40%–70%	0.76	0.624 ± 0.062 ± 5.1	2.73 ± 0.16 ± 5.3	2.67 ± 0.16 ± 2.5	2.35 ± 0.15 ± 8.3
	0.91	0.565 ± 0.065 ± 14.6	2.33 ± 0.17 ± 9.8	2.44 ± 0.16 ± 5.5	1.97 ± 0.17 ± 15.4
	1.09	0.575 ± 0.068 ± 19.5	2.08 ± 0.17 ± 5.8	2.03 ± 0.19 ± 5.3	1.54 ± 0.16 ± 8

TABLE VII. R_o/R_s of positive and negative pion pairs plus charge-combined kaon pairs, shown as value ± statistical uncertainty (absolute value) ± systematic uncertainty (%), for the centrality bins shown in Fig. 4.

Meson pair	$\langle m_T \rangle$ (GeV/c)	R_o/R_s 0%–10%	10%–20%	20%–40%	40%–70%
$\pi^+\pi^+$	0.3	1.09 ± 0.01 ± 3.3	1.08 ± 0.01 ± 2.3	1.06 ± 0.01 ± 2.1	1.04 ± 0.01 ± 1.9
	0.36	1.10 ± 0.01 ± 3.5	1.10 ± 0.01 ± 3.0	1.07 ± 0.01 ± 1.6	1.08 ± 0.01 ± 1.7
	0.41	1.09 ± 0.01 ± 3.5	1.08 ± 0.01 ± 3.0	1.07 ± 0.01 ± 2.1	1.08 ± 0.01 ± 2.4
	0.47	1.05 ± 0.01 ± 4.3	1.04 ± 0.01 ± 3.6	1.03 ± 0.01 ± 2.5	1.03 ± 0.01 ± 0.9
	0.53	1.01 ± 0.01 ± 3.8	1.01 ± 0.01 ± 2.3	1.00 ± 0.01 ± 2.2	1.03 ± 0.02 ± 1.1
	0.59	1.00 ± 0.01 ± 5.6	1.00 ± 0.01 ± 3.7	0.98 ± 0.01 ± 2.6	0.99 ± 0.02 ± 1.4
	0.66	0.96 ± 0.01 ± 5.6	0.96 ± 0.01 ± 4.7	0.95 ± 0.01 ± 2.9	0.95 ± 0.02 ± 3.2
	0.79	0.94 ± 0.01 ± 5.4	0.93 ± 0.01 ± 5.5	0.92 ± 0.01 ± 4.7	0.89 ± 0.02 ± 1.5
	0.96	0.92 ± 0.03 ± 10.7	0.94 ± 0.03 ± 5.0	0.89 ± 0.02 ± 4.5	0.85 ± 0.03 ± 3.7
	1.16	0.82 ± 0.05 ± 7.8	0.81 ± 0.05 ± 11.9	0.89 ± 0.04 ± 2.9	0.81 ± 0.08 ± 10.5
$\pi^-\pi^-$	0.3	1.07 ± 0.01 ± 3.3	1.07 ± 0.01 ± 3.2	1.04 ± 0.01 ± 2.1	1.02 ± 0.01 ± 1.5
	0.36	1.11 ± 0.01 ± 2.5	1.10 ± 0.01 ± 3.2	1.05 ± 0.01 ± 1.9	1.07 ± 0.02 ± 2.4
	0.41	1.09 ± 0.01 ± 3.9	1.07 ± 0.01 ± 3.1	1.07 ± 0.01 ± 1.2	1.08 ± 0.02 ± 1.6
	0.47	1.02 ± 0.01 ± 4.3	1.04 ± 0.01 ± 3.2	1.03 ± 0.01 ± 2.7	1.04 ± 0.02 ± 2.1
	0.53	1.01 ± 0.01 ± 4.3	1.03 ± 0.01 ± 3.4	0.99 ± 0.01 ± 1.3	0.99 ± 0.02 ± 1.6
	0.59	0.99 ± 0.01 ± 5.4	0.99 ± 0.01 ± 3.9	0.98 ± 0.01 ± 3.0	0.99 ± 0.02 ± 4.4
	0.66	0.96 ± 0.01 ± 5.5	0.96 ± 0.01 ± 4.9	0.95 ± 0.01 ± 3.2	0.96 ± 0.02 ± 1.9
	0.79	0.91 ± 0.01 ± 6.7	0.92 ± 0.01 ± 4.3	0.91 ± 0.01 ± 2.9	0.91 ± 0.02 ± 2.0
	0.96	0.86 ± 0.03 ± 5.0	0.93 ± 0.03 ± 4.3	0.87 ± 0.02 ± 3.8	0.85 ± 0.04 ± 3.3
	1.15	0.73 ± 0.05 ± 8.7	0.86 ± 0.06 ± 7.6	0.8 ± 0.05 ± 4.8	0.79 ± 0.09 ± 6.7
$K^+K^+ + K^-K^-$	0.76	1.07 ± 0.06 ± 5.3	1.06 ± 0.06 ± 4.5	1.03 ± 0.05 ± 5.3	0.98 ± 0.08 ± 7.1
	0.91	1.05 ± 0.06 ± 8.9	1.06 ± 0.06 ± 2.9	1.01 ± 0.05 ± 3.6	1.05 ± 0.10 ± 6.1
	1.1	1.08 ± 0.08 ± 5.2	0.90 ± 0.07 ± 3.8	0.90 ± 0.07 ± 3.1	0.98 ± 0.12 ± 2.3

TABLE VIII. Azimuthal angle dependence of HBT radii of charged pions, shown as value ± statistical uncertainty (absolute value) ± systematic uncertainty (%), for the 0%–20% and 20%–60% centrality bins.

Centrality	k_T (GeV/c)	$\phi - \Psi_2$ (rad)	R_s^2 (fm^2)	R_o^2 (fm^2)	R_l^2 (fm^2)	R_{os}^2 (fm^2)
0%–20%	0.2–0.3	0	23.68 ± 0.27 ± 0.56	25.25 ± 0.34 ± 1.54	34.72 ± 0.48 ± 1.97	0.21 ± 0.2 ± 0.11
		$\pi/4$	22.88 ± 0.27 ± 0.56	27.33 ± 0.37 ± 1.79	35.05 ± 0.49 ± 1.63	2.53 ± 0.21 ± 0.25
		$\pi/2$	22.46 ± 0.27 ± 0.56	30.65 ± 0.42 ± 1.8	35.34 ± 0.51 ± 0.98	0.26 ± 0.23 ± 0.27
		$3\pi/4$	23.4 ± 0.28 ± 0.51	28.06 ± 0.39 ± 1.31	35.46 ± 0.51 ± 1.41	−2.01 ± 0.22 ± 0.24
	0.3–0.4	0	20.5 ± 0.2 ± 0.67	21.87 ± 0.24 ± 1.38	24.44 ± 0.29 ± 1.64	0.22 ± 0.14 ± 0.13
		$\pi/4$	19.82 ± 0.21 ± 0.4	24.09 ± 0.27 ± 1.2	24.03 ± 0.3 ± 1.52	2.38 ± 0.15 ± 0.26
		$\pi/2$	18.38 ± 0.2 ± 0.67	26.93 ± 0.31 ± 2.02	24.28 ± 0.31 ± 1.38	0.59 ± 0.16 ± 0.34
		$3\pi/4$	19.16 ± 0.2 ± 0.35	23.96 ± 0.27 ± 1.78	24.35 ± 0.3 ± 1.3	−2.01 ± 0.15 ± 0.31
	0.4–0.5	0	17.36 ± 0.18 ± 0.5	16.61 ± 0.2 ± 1.15	16.81 ± 0.21 ± 1.31	0.06 ± 0.12 ± 0.2
		$\pi/4$	17.01 ± 0.19 ± 0.42	18.58 ± 0.23 ± 1.41	17.42 ± 0.23 ± 1.59	2.11 ± 0.13 ± 0.18
		$\pi/2$	15.76 ± 0.19 ± 0.32	20.46 ± 0.27 ± 1.55	17.73 ± 0.25 ± 1.16	0.31 ± 0.14 ± 0.19
		$3\pi/4$	16.55 ± 0.19 ± 0.23	18.51 ± 0.23 ± 1.25	17.26 ± 0.23 ± 1.29	−1.79 ± 0.13 ± 0.17
	0.5–0.6	0	15.78 ± 0.19 ± 0.45	13.22 ± 0.19 ± 1.05	13.85 ± 0.21 ± 0.68	0.1 ± 0.12 ± 0.25
		$\pi/4$	15.32 ± 0.2 ± 0.42	15.34 ± 0.23 ± 1.42	14.25 ± 0.23 ± 0.88	1.82 ± 0.13 ± 0.28
		$\pi/2$	13.75 ± 0.2 ± 0.39	17.22 ± 0.28 ± 1.31	14.18 ± 0.25 ± 0.74	0.16 ± 0.14 ± 0.25
		$3\pi/4$	14.84 ± 0.19 ± 0.43	14.32 ± 0.22 ± 1.4	13.85 ± 0.22 ± 0.72	−1.36 ± 0.12 ± 0.24
	0.6–0.8	0	13.87 ± 0.18 ± 0.4	10.11 ± 0.16 ± 1.04	9.81 ± 0.16 ± 0.49	0.04 ± 0.1 ± 0.1
		$\pi/4$	12.33 ± 0.17 ± 0.35	11.16 ± 0.18 ± 0.94	9.88 ± 0.17 ± 1.06	1.44 ± 0.11 ± 0.26
		$\pi/2$	11.28 ± 0.17 ± 0.2	12.01 ± 0.21 ± 1.26	10.51 ± 0.19 ± 1.24	0.18 ± 0.11 ± 0.2
		$3\pi/4$	12.35 ± 0.17 ± 0.28	10.59 ± 0.18 ± 0.78	9.99 ± 0.17 ± 0.61	−1.23 ± 0.1 ± 0.17
	0.8–1.5	0	11.04 ± 0.24 ± 0.36	6.85 ± 0.19 ± 0.88	6.37 ± 0.17 ± 0.74	−0.07 ± 0.12 ± 0.19
		$\pi/4$	9.83 ± 0.23 ± 0.31	7.57 ± 0.23 ± 0.68	6.05 ± 0.18 ± 0.73	1.19 ± 0.13 ± 0.15
		$\pi/2$	7.92 ± 0.21 ± 0.52	8.61 ± 0.28 ± 0.74	5.64 ± 0.19 ± 0.44	0.06 ± 0.13 ± 0.23
		$3\pi/4$	9.74 ± 0.25 ± 0.37	7.04 ± 0.21 ± 0.78	6.2 ± 0.18 ± 0.48	−1.28 ± 0.13 ± 0.18
20%–60%	0.2–0.3	0	16.24 ± 0.19 ± 0.29	14.53 ± 0.21 ± 0.84	22.44 ± 0.32 ± 0.97	0.27 ± 0.13 ± 0.25
		$\pi/4$	15.18 ± 0.19 ± 0.28	16.97 ± 0.24 ± 0.85	22.64 ± 0.33 ± 0.7	2.3 ± 0.14 ± 0.3
		$\pi/2$	12.81 ± 0.17 ± 0.24	18.97 ± 0.28 ± 0.88	21.85 ± 0.34 ± 0.76	0.3 ± 0.14 ± 0.34
		$3\pi/4$	14.79 ± 0.18 ± 0.33	16.34 ± 0.24 ± 0.95	22.47 ± 0.33 ± 0.52	−1.8 ± 0.13 ± 0.35
	0.3–0.4	0	13.98 ± 0.15 ± 0.27	12.92 ± 0.14 ± 0.62	15.9 ± 0.2 ± 0.59	0.09 ± 0.09 ± 0.15
		$\pi/4$	13.15 ± 0.15 ± 0.22	15.38 ± 0.18 ± 0.79	15.77 ± 0.21 ± 0.46	2.82 ± 0.1 ± 0.12
		$\pi/2$	11.04 ± 0.13 ± 0.26	17.49 ± 0.22 ± 0.74	15.11 ± 0.21 ± 0.52	0.31 ± 0.11 ± 0.15
		$3\pi/4$	12.56 ± 0.14 ± 0.18	15.03 ± 0.17 ± 0.74	15.19 ± 0.2 ± 0.63	−2.4 ± 0.1 ± 0.16
	0.4–0.5	0	12.58 ± 0.14 ± 0.17	10.22 ± 0.12 ± 0.58	11.31 ± 0.15 ± 0.45	0.17 ± 0.08 ± 0.18
		$\pi/4$	11.55 ± 0.14 ± 0.22	12.12 ± 0.15 ± 0.64	11.31 ± 0.16 ± 0.51	2.49 ± 0.09 ± 0.14
		$\pi/2$	9.32 ± 0.13 ± 0.28	14.99 ± 0.21 ± 0.82	11.39 ± 0.18 ± 0.63	0.17 ± 0.1 ± 0.13
		$3\pi/4$	11.05 ± 0.13 ± 0.26	12.25 ± 0.16 ± 0.58	11.72 ± 0.17 ± 0.59	−2.04 ± 0.09 ± 0.19
	0.5–0.6	0	11.28 ± 0.14 ± 0.17	8.22 ± 0.12 ± 0.47	9.08 ± 0.14 ± 0.29	0.09 ± 0.09 ± 0.1
		$\pi/4$	10.15 ± 0.14 ± 0.29	9.83 ± 0.15 ± 0.48	9.38 ± 0.16 ± 0.39	2.21 ± 0.09 ± 0.18
		$\pi/2$	8.12 ± 0.14 ± 0.27	12.04 ± 0.21 ± 0.56	8.96 ± 0.18 ± 0.49	−0.03 ± 0.1 ± 0.16
		$3\pi/4$	10.09 ± 0.14 ± 0.24	10.2 ± 0.16 ± 0.64	9.07 ± 0.16 ± 0.41	−2.05 ± 0.09 ± 0.13
	0.6–0.8	0	9.57 ± 0.12 ± 0.21	6.08 ± 0.09 ± 0.4	6.53 ± 0.1 ± 0.31	0 ± 0.06 ± 0.06
		$\pi/4$	8.55 ± 0.13 ± 0.12	7.68 ± 0.13 ± 0.41	6.46 ± 0.12 ± 0.25	1.82 ± 0.07 ± 0.12
		$\pi/2$	6.71 ± 0.12 ± 0.31	9.47 ± 0.18 ± 0.47	6.61 ± 0.14 ± 0.27	0.16 ± 0.08 ± 0.14
		$3\pi/4$	8.62 ± 0.13 ± 0.26	7.56 ± 0.13 ± 0.45	6.57 ± 0.12 ± 0.44	−1.82 ± 0.07 ± 0.16
	0.8–1.5	0	7.81 ± 0.16 ± 0.27	4.2 ± 0.1 ± 0.29	4 ± 0.1 ± 0.2	0 ± 0.07 ± 0.1
		$\pi/4$	7.18 ± 0.18 ± 0.33	5.06 ± 0.15 ± 0.27	4.3 ± 0.13 ± 0.24	1.47 ± 0.09 ± 0.12
		$\pi/2$	4.74 ± 0.16 ± 0.22	6.72 ± 0.26 ± 0.68	3.84 ± 0.15 ± 0.65	0.34 ± 0.1 ± 0.2
		$3\pi/4$	6.58 ± 0.17 ± 0.36	5.36 ± 0.16 ± 0.25	3.94 ± 0.12 ± 0.45	−1.32 ± 0.09 ± 0.09

TABLE IX. Azimuthal angle dependence of HBT radii of charged kaons, shown as value ± statistical uncertainty (absolute value) ± systematic uncertainty (%), for the centrality bins shown in Fig. 8.

Centrality	$\phi - \Psi_2$ (rad)	R_s^2 (fm^2)	R_o^2 (fm^2)	R_l^2 (fm^2)	R_{os}^2 (fm^2)
0%–20%	0	11.86 ± 0.68 ± 0.42	10.77 ± 0.79 ± 1.14	10.43 ± 0.72 ± 1.34	1.22 ± 0.58 ± 0.77
	$\pi/4$	10.02 ± 0.57 ± 1.04	11.89 ± 0.82 ± 1.22	8.74 ± 0.61 ± 1.70	2.43 ± 0.52 ± 0.65
	$\pi/2$	7.98 ± 0.47 ± 0.92	13.29 ± 0.97 ± 1.96	9.25 ± 0.64 ± 1.47	−1.31 ± 0.52 ± 0.42
	$3\pi/4$	10.67 ± 0.61 ± 0.66	12.45 ± 0.90 ± 0.86	9.44 ± 0.65 ± 1.09	−2.15 ± 0.61 ± −0.69
20%–60%	0	10 ± 0.58 ± 0.69	7.49 ± 0.54 ± 0.69	5.71 ± 0.40 ± 0.6	0.28 ± 0.44 ± 0.22
	$\pi/4$	7.52 ± 0.46 ± 0.56	8.03 ± 0.58 ± 0.69	6.07 ± 0.43 ± 0.71	2.05 ± 0.40 ± 0.29
	$\pi/2$	4.69 ± 0.31 ± 0.68	8.56 ± 0.59 ± 0.99	5.61 ± 0.42 ± 0.81	0.41 ± 0.34 ± 0.25
	$3\pi/4$	8.03 ± 0.49 ± 0.65	8.51 ± 0.62 ± 0.77	5.27 ± 0.40 ± 0.83	−1.52 ± 0.43 ± −0.24

TABLE X. Oscillation amplitudes relative to the event plane for charged pions, shown as value ± statistical uncertainty (absolute value) ± systematic uncertainty (%), for the 0%–20% and 20%–60% centrality bins.

Centrality	m_T (GeV/c)	R_s^2 (fm^2)	R_o^2 (fm^2)	R_l^2 (fm^2)	R_{os}^2 (fm^2)
0%–20%	0.30	0.026 ± 0.007 ± 0.015	0.095 ± 0.008 ± 0.024	0.114 ± 0.010 ± 0.029	0.099 ± 0.007 ± 0.009
	0.38	0.054 ± 0.006 ± 0.032	0.101 ± 0.007 ± 0.018	0.125 ± 0.008 ± 0.025	0.113 ± 0.005 ± 0.013
	0.47	0.046 ± 0.007 ± 0.018	0.104 ± 0.008 ± 0.025	0.116 ± 0.008 ± 0.030	0.117 ± 0.006 ± 0.010
	0.57	0.065 ± 0.008 ± 0.027	0.125 ± 0.009 ± 0.020	0.126 ± 0.009 ± 0.024	0.107 ± 0.006 ± 0.016
	0.70	0.106 ± 0.008 ± 0.015	0.082 ± 0.010 ± 0.032	0.072 ± 0.009 ± 0.028	0.107 ± 0.006 ± 0.016
	0.93	0.160 ± 0.014 ± 0.040	0.098 ± 0.019 ± 0.040	0.077 ± 0.015 ± 0.022	0.129 ± 0.010 ± 0.013
20%–60%	0.30	0.114 ± 0.007 ± 0.009	0.131 ± 0.009 ± 0.024	0.149 ± 0.010 ± 0.027	0.140 ± 0.007 ± 0.022
	0.38	0.113 ± 0.007 ± 0.019	0.150 ± 0.007 ± 0.015	0.181 ± 0.008 ± 0.020	0.207 ± 0.006 ± 0.010
	0.47	0.144 ± 0.007 ± 0.017	0.180 ± 0.008 ± 0.015	0.201 ± 0.009 ± 0.019	0.205 ± 0.006 ± 0.012
	0.57	0.155 ± 0.008 ± 0.022	0.185 ± 0.010 ± 0.011	0.189 ± 0.010 ± 0.011	0.216 ± 0.007 ± 0.014
	0.70	0.165 ± 0.009 ± 0.029	0.212 ± 0.010 ± 0.021	0.196 ± 0.010 ± 0.018	0.220 ± 0.007 ± 0.017
	0.93	0.226 ± 0.015 ± 0.026	0.211 ± 0.019 ± 0.027	0.172 ± 0.016 ± 0.021	0.216 ± 0.010 ± 0.012

TABLE XI. Oscillation amplitudes relative to the event plane for charged kaons, ± systematic uncertainty (%) for the 0%–20% and 20%–60% centrality bins shown in Fig. 12.

Centrality	m_T (GeV/c)	R_s^2 (fm^2)	R_o^2 (fm^2)	R_l^2 (fm^2)	R_{os}^2 (fm^2)
0%–20%	0.91	0.193 ± 0.034 ± 0.078	0.106 ± 0.044 ± 0.033	0.128 ± 0.052 ± 0.044	0.227 ± 0.040 ± 0.067
20%–60%	0.91	0.360 ± 0.035 ± 0.080	0.070 ± 0.042 ± 0.035	0.076 ± 0.045 ± 0.038	0.238 ± 0.040 ± 0.030

[1] K. Adcox *et al.* (PHENIX Collaboration), Formation of dense partonic matter in relativistic nucleus-nucleus collisions at RHIC: Experimental evaluation by the PHENIX collaboration, Nucl. Phys. A **757**, 184 (2005).

[2] J. Adams *et al.* (STAR Collaboration), Experimental and theoretical challenges in the search for the quark gluon plasma: The STAR Collaboration's critical assessment of the evidence from RHIC collisions, Nucl. Phys. A **757**, 102 (2005).

[3] B. B. Back *et al.* (PHOBOS Collaboration), The PHOBOS perspective on discoveries at RHIC, Nucl. Phys. A **757**, 28 (2005).

[4] L. Arsene *et al.* (BRAHMS Collaboration), Quark gluon plasma and color glass condensate at RHIC? The perspective from the BRAHMS experiment, Nucl. Phys. A **757**, 1 (2005).

[5] K. Aamodt *et al.* (ALICE Collaboration), Suppression of charged particle production at large transverse momentum in central Pb+Pb collisions at $\sqrt{s_{NN}} = 2.76$ TeV, Phys. Lett. B **696**, 30 (2011).

[6] S. Chatrchyan *et al.* (CMS Collaboration), Observation and studies of jet quenching in PbPb collisions at $\sqrt{s_{NN}} = 2.76$ TeV, Phys. Rev. C **84**, 024906 (2011).

[7] G. Aad *et al.* (ATLAS Collaboration), Observation of a Centrality-Dependent Dijet Asymmetry in Lead-Lead Collisions at $\sqrt{s_{NN}} = 2.76$ TeV with the ATLAS Detector at the LHC, Phys. Rev. Lett. **105**, 252303 (2010).

[8] W. A. Zajc *et al.*, Two-pion correlations in heavy ion collisions, Phys. Rev. C **29**, 2173 (1984).

[9] M. Lisa, S. Pratt, R. Soltz, and U. Wiedemann, Femtoscopy in relativistic heavy ion collisions: Two decades of progress, Annu. Rev. Nucl. Part. Sci. **55**, 357 (2005).

[10] R. Hanbury Brown and R. Q. Twiss, A test of a new type of stellar interferometer on Sirius, Nature (London) **178**, 1046 (1956).

[11] G. Goldhaber, S. Goldhaber, W. Lee, and A. Pais, Influence of Bose-Einstein statistics on the antiproton-proton annihilation process, Phys. Rev. **120**, 300 (1960).

[12] S. S. Adler *et al.* (PHENIX Collaboration), Bose-Einstein Correlations of Charged Pion Pairs in Au+Au Collisions at $\sqrt{s_{NN}} = 200$ GeV, Phys. Rev. Lett. **93**, 152302 (2004).

[13] S. Pratt, Resolving the Hanbury Brown–Twiss Puzzle in Relativistic Heavy Ion Collisions, Phys. Rev. Lett. **102**, 232301 (2009).

[14] S. Afanasiev *et al.* (PHENIX Collaboration), Charged Kaon Interfrometrci Probes of Space-Time Evolution in Au+Au Collisions at $\sqrt{s_{NN}} = 200$ GeV, Phys. Rev. Lett. **103**, 142301 (2009).

[15] L. Adamczyk *et al.* (STAR Collaboration), Freeze-out dynamics via charged kaon femtoscopy in $\sqrt{s_{NN}} = 200$ GeV central Au+Au collisions, Phys. Rev. C **88**, 034906 (2013).

[16] M. P. Szymanski *et al.* (ALICE Collaboration), Meson and baryon femtoscopy in heavy-ion collisions at ALICE, Nucl. Phys. A **904-905**, 447c (2013).

[17] J. P. Sullivan, M. Berenguer, D. E. Fields, B. V. Jacak, M. Sarabura, J. Simon-Gillo, H. Sorge, H. van Hecke, and S. Pratt, Calculations of Bose-Einstein correlations from relativistic quantum molecular dynamics, Nucl. Phys. A **566**, 531 (1994).

[18] J. P. Sullivan, M. Berenguer, B. V. Jacak, S. Pratt, M. Sarabura, J. Simon-Gillo, H. Sorge, and H. van Hecke, Bose-Einstein Correlations of Pion Pairs and Kaon Pairs from Relativistic Quantum Molecular Dynamics, Phys. Rev. Lett. **70**, 3000 (1993).

[19] M. A. Lisa *et al.* (E895 Collaboration), Azimuthal dependence of pion interferometry at the AGS, Phys. Lett. B **496**, 1 (2000).

[20] D. Adamov'a *et al.* (CERES Collaboration), Azimuthal dependence of pion source radii in Pb+Au collisions at 158 A GeV/c, Phys. Rev. C **78**, 064901 (2008).

[21] J. Adams *et al.* (STAR Collaboration), Azimuthally Sensitive Hanbury Brown–Twiss Interferometry in Au+Au Collisions at $\sqrt{s_{NN}} = 200$ GeV, Phys. Rev. Lett. **93**, 012301 (2004).

[22] A. Adare *et al.* (PHENIX Collaboration), Azimuthal-Angle Dependence of Charged-Pion-Interferometry Measurements with Respect to 2$^{\text{nd}}$- and 3$^{\text{rd}}$- Event Planes in Au+Au Collisions at $\sqrt{s_{NN}} = 200$ GeV, Phys. Rev. Lett. **112**, 222301 (2014).

[23] K. Adcox *et al.* (PHENIX Collaboration), PHENIX detector overview, Nucl. Instrum. Methods Phys. Res., Sect. A **499**, 469 (2003).

[24] M. Allen *et al.* (PHENIX Collaboration), PHENIX inner detectors, Nucl. Instrum. Methods Phys. Res., Sect. A **499**, 549 (2003).

[25] E. Richardson *et al.* (PHENIX Collaboration), A reaction plane detector for PHENIX at RHIC, Nucl. Instrum. Methods Phys. Res., Sect. A **636**, 99 (2011).

[26] A. Adare *et al.* (PHENIX Collaboration), Deviation from quark number scaling of the anisotropy parameter v2 of pions, kaons, and protons in Au+Au collisions at $\sqrt{s_{NN}} = 200$ GeV, Phys. Rev. C **85**, 064914 (2012).

[27] L. Aphecetche *et al.* (PHENIX Collaboration), PHENIX calorimeter, Nucl. Instrum. Methods Phys. Res., Sect. A **499**, 521 (2003).

[28] A. Adare *et al.*, Spectra and ratios of identified particles in Au+Au and d+Au collisions at $\sqrt{s_{NN}} = 200$ GeV, Phys. Rev. C **88**, 024906 (2013).

[29] S. Pratt, Coherence and Coulomb effects on pion interferometry, Phys. Rev. D **33**, 72 (1986).

[30] G. Bertsch, M. Gong, and M. Tohyama, Pion interferometry in ultra relativistic heavy-ion collisions, Phys. Rev. C **37**, 1896 (1988).

[31] M. G. Bowler, Coulomb corrections to Bose-Einstein corrections have been greatly exaggerated, Phys. Lett. B **270**, 69 (1991).

[32] Y. M. Sinyukov, R. Lednickya, S. V. Akkelinb, J. Plutaa, and B. Erazmus, Coulomb corrections for interferometry analysis of expanding hadron systems, Phys. Lett. B **432**, 248 (1998).

[33] S. Afanasiev *et al.* (PHENIX Collaboration), Systematic studies of elliptic flow measurements in Au+Au collisions at $\sqrt{s_{NN}} =$ 200 GeV, Phys. Rev. C **80**, 024909 (2009).

[34] A. M. Poskanzer and S. A. Voloshin, Methods for analyzing anisotropic flow in relativistic nuclear collisions, Phys. Rev. C **58**, 1671 (1998).

[35] F. Retière and M. A. Lisa, Observable implications of geometrical and dynamical aspects of freeze-out in heavy ion collisions, Phys. Rev. C **70**, 044907 (2004).

[36] C. Alt *et al.* (NA49 Collaboration), Bose-Einstein correlations of $\pi^-\pi^-$ pairs in central Pb+Pb collisions at 20A, 30A, 40A, 80A, and 158A GeV, Phys. Rev. C **77**, 064908 (2008).

[37] J. Adams *et al.* (STAR Collaboration), Pion Interferometry in Au+Au Collisions at $\sqrt{s_{NN}} = 200$ GeV, Phys. Rev. C **71**, 044906 (2005).

[38] Y. M. Sinyukov and V. M. Shapoval (private communication); I. A. Karpenko, Y. M. Sinyukov, and K. Werner, Uniform description of bulk observables in the hydrokinetic model of

A+A collisions at the BNL Relativistic Heavy Ion Collider and the CERN Large Hadron Collider, Phys. Rev. C **87**, 024914 (2013).

[39] P. Bożek, Azimuthally sensitive femtoscopy in event-by-event hydrodynamics, Phys. Rev. C **89**, 044904 (2014).

[40] M. Csanád and T. Csörgő, Kaon HBT radii from perfect fluid dynamics using the Buda-Lund model, Acta Phys. Polon. Supp. **1**, 521 (2008).

[41] I. A. Karpenko and Y. M. Sinyukov, Kaon and pion femtoscopy at the highest energies available at the BNL Relativistic Heavy Ion Collider (RHIC) in a hydrokinetic model, Phys. Rev. C **81**, 054903 (2010).

[42] V. M. Shapoval, P. Braun-Munzinger, I. A. Karpenko, and Y. M. Sinyukov, Femtoscopy correlations of kaons in Pb+Pb collisions at LHC within hydrokinetic model, Nucl. Phys. A **929**, 1 (2014).

[43] S. V. Akkelin and Y. M. Sinyukov, The HBT-interferometry of expanding inhomogeneous sources, Z. Phys. C **72**, 501 (1996).

[44] J. Beringer *et al.* (Particle Data Group Collaboration), Review of particle physics (RPP), Phys. Rev. D **86**, 010001 (2012).

[45] E. Frodermann, R. Chatterjee, and U. Heinz, Evolution of pion HBT radii from RHIC to LHC: Predictions from ideal hydrodynamics, J. Phys. G: Nucl. Part. Phys. **34**, 2249 (2007).

[46] U. Heinz, A. Hummel, M. A. Lisa, and U. A. Wiedemann, Symmetry constraints for the emission angle dependence of Hanbury-Brown-Twiss radii, Phys. Rev. C **66**, 044903 (2002).

[47] E. Schnedermann, J. Sollfrank, and U. Heinz, Thermal phenomenology of hadrons from 200A GeV S+S collisions, Phys. Rev. C **48**, 2462 (1993).

[48] S. S. Adler *et al.* (PHENIX Collaboration), Identified charged particle spectra and yields in Au+Au collisions at $\sqrt{s_{NN}} =$ 200 GeV, Phys. Rev. C **69**, 034909 (2004).

[49] A. Adare *et al.* (PHENIX Collaboration), Systematic study of azimuthal anisotropy in Cu+Cu and Au+Au collisions at $\sqrt{s_{NN}} = 62.4$ and 200 GeV, Phys. Rev. C **92**, 034913 (2015).

[50] S. S. Adler *et al.* (PHENIX Collaboration), Production of ϕ mesons at mid rapidity in $\sqrt{s_{NN}} = 200$ GeV Au+Au collisions at relativistic energies, Phys. Rev. C **72**, 014903 (2005).

[51] P. Bożek, Flow and interferometry in (3+1)-dimensional viscous hydrodynamics, Phys. Rev. C **85**, 034901 (2012).